Single-step probabilistic inversion of 3D seismic data of a carbonate reservoir in Southwest Iran

Akbar Heidari[1,1,1], Thomas Mejer Hansen[2,2,2], Hamed Amini[3,3,3], Mohammad Emami-Niri[4,5,5], Rasmus Bødker Madsen[6,6,6], and Navid Amini[7,7,7]

[1]University of Tehran, Institute of Geophysics
[2]Aarhus University,Aarhus University,University of Aarhus
[3]AkerBP
[4]Institute of Petroleum Engineering, College of Engineering, University of Tehran
[5]Institute of Petroleum Engineering
[6]Geological Survey of Denmark and Greenland
[7]CoCoLink, subsidiary of Seoul National University, Republic of Korea

November 30, 2022

Abstract

We use a sampling-based Markov chain Monte Carlo method to invert seismic data directly to porosity and quantify its uncertainty distribution in a hard-rock carbonate reservoir in Southwest Iran. Due to the processing of the seismic data, the remainder noise is correlated with the bandwidth in the range of the seismic wavelet. Hence, we assume the estimated seismic wavelet as a suitable proxy for capturing the coupling of noise samples and we propose a simple and pragmatic approach to account for the correlated (colored) noise in the probabilistic inversion of real seismic data. We also calibrate an empirical and a semi-empirical inclusion-based rock-physics model to characterize the rock-frame elastic moduli via lithology constrained fitting parameters of these models, i.e. the critical porosity and the pore aspect ratio. These calibrated rock-physics models are embedded in the inversion procedure to link petrophysical and elastic properties. In addition, we obtain the pointwise critical porosity and pore aspect ratio, which can potentially facilitate the interpretation of the reservoir for further studies. The inversion results are evaluated by comparing with porosity logs and an existing geological model (porosity model) constructed through a geostatistical simulation approach. We assess the consistency of the geological model through a geomodel-to-seismic modeling approach. The results confirm the performance of the probabilistic inversion in resolving some thin layers and reconstructing the observed seismic data. We also present the applicability of the proposed sampling-based approach to invert 3D seismic data for estimating the porosity distribution and its associated uncertainty for four subzones of the reservoir. The porosity time maps and the facies probabilities obtained via porosity cut-offs indicate the relative quality of the reservoir's subzones over each other.

ABSTRACT

We use a sampling-based Markov chain Monte Carlo method to invert seismic data directly to porosity and quantify its uncertainty distribution in a hard-rock carbonate reservoir in Southwest Iran. Due to the processing of the seismic data, the remainder noise is correlated with the bandwidth in the range of the seismic wavelet. Hence, we assume the estimated seismic wavelet as a suitable proxy for capturing the coupling of noise samples and we propose a simple and pragmatic approach to account for the correlated (colored) noise in the probabilistic inversion of real seismic data. We also calibrate an empirical and a semi-empirical inclusion-based rock-physics model to characterize the rock-frame elastic moduli via lithology constrained fitting parameters of these models, i.e. the critical porosity and the pore aspect ratio. These calibrated rock-physics models are embedded in the inversion procedure to link petrophysical and elastic properties. In addition, we obtain the pointwise critical porosity and pore aspect ratio, which can potentially facilitate the interpretation of the reservoir for further studies. The inversion results are evaluated by comparing with porosity logs and an existing geological model (porosity model) constructed through a geostatistical simulation approach. We assess the consistency of the geological model through a geomodel-to-seismic modeling approach. The results confirm the performance of the probabilistic inversion in resolving some thin layers and reconstructing the observed seismic data. We also present the applicability of the proposed sampling-based approach to invert 3D seismic data for estimating the porosity distribution and its associated uncertainty for four subzones of the reservoir. The porosity time maps and the facies probabilities obtained via porosity cut-offs indicate the relative quality of the reservoir's subzones over each other.

INTRODUCTION

Describing the vertical and spatial variability of reservoir properties such as porosity around target zones is the holy grail of seismic hydrocarbon reservoir characterization. This challenge is addressed by quantitative integration of the seismic and well log data to map the distribution of the reservoir properties. From a mathematical point of view, this procedure is an ill-posed inverse problem. There are two distinct approaches to solve this inverse problem. The deterministic approach, in which by minimizing a cost function over the observed and modeled data residuals, a single "optimal" solution is produced (Aster et al., 2018). In probabilistic approaches, many realizations of the reservoir properties, e.g., porosity are produced, which can fit the observed data within the noise (Tarantola and Valette, 1982). The procedure of seismic data inversion to the reservoir properties is commonly a two-step approach (Goodway et al., 1997). First, the seismic data is inverted to the elastic parameters, then the inverted elastic properties are converted to petrophysical properties using a calibrated rock-physics model (RPM) (Aleardi, 2018; Aleardi et al., 2018; Ghon et al., 2020). Doyen (2007) argue that the two-step methods cannot guarantee the consistency between the seismic response from the estimated reservoir properties and the observed seismic data. To get around these issues, the RPM can be included in the seismic inversion methods (Gunning and Glinsky, 2004; Kolbjørnsen et al., 2020). This approach is known as the single-step inversion. Gradient-based inversion approaches such as Gauss-Newton, steepest descent as well as stochastic optimization methods (i.e., simulated annealing, particle swarm, and genetic algorithm) are commonly used to solve the nonlinear inverse problems (Sajeva et al., 2017; Aster, 2018). One of the drawbacks of the gradient-based methods is linearizing the problem around an initial model that the solution may converge to a local minimum. This can lead to an underestimation of the uncertainty related to the final obtained model. However, these approaches are often used due to their limited computational costs. In contrast, the stochastic optimization approaches are less prone to get trapped in local minima, but their computational costs increase with the number of model parameters. The uncertainty in seismic inversion is generally associated with the limited bandwidth of the seismic data and the noise in the seismic data, which is attributed to the measurement errors as well as the errors associated with the imperfect forward model and/or simplified parametrizations (Tarantola, 2005). The other source of uncertainty is the intrinsic variability of the petrophysical properties and insufficient data sampling through wells that are typically spaced kilometers apart or centimeter-scale core measurements. One of the practical motivations for uncertainty quantification is for risk analysis and optimal decision-making for reservoir characterization and well planning studies. Bayesian approaches could reasonably quantify the uncertainty of the target model parameters (Malinverno and Briggs, 2004; Tarantola, 2005; Talarico et al., 2020). In the context of seismic reservoir characterization studies, the solution of the probabilistic formulation of an inverse problem is a posterior distribution of the petrophysical properties conditioned by the observed data, at each time/depth location of the reservoir model. The posterior distribution describes, in principle, all the models that lead to a data fit within the noise, and hence allows a full description of the uncertainty of the model parameters.

Regarding the crucial role of the rock-physics relations in single-step petrophysical seismic inversion approaches, the combination of Bayesian formulation and rock-physics modeling to estimate the probability distribution of the reservoir properties given seismic data are proposed as a practical approach in reservoir characterization studies. The proposed methodologies vary in different aspects such as statistical assumptions (i.e., Gaussian, Gaussian mixture, Generalized Gaussian or non-parametric PDFs (Grana et al., 2017; Fjeldstad and Grana, 2018; Grana, 2020; Kolbjørnsen et al., 2020)), the computational algorithms (analytical solutions versus numerical (Monte Carlo) methods (Gunning and Sams, 2018)), physical models (linearized or nonlinear rock physics and seismic forward modeling operators (Grana, 2016)), and model variables (facies, petroelastic or petrophysical properties (Grana and Della Rossa, 2010; Rimstad et al., 2012)). Buland and Omre (2003) explicitly warn about using too-informed priors. On the other hand, it is argued that oversimplification of the prior models and forward operators could provide a biased estimation of model parameters with deceptive uncertainties (Madsen and Hansen, 2018). In these cases, it is highly acknowledged to use sampling methods. These methods can handle, in principle, nonlinear forward models, arbitrarily complex prior and noise models. Importance sampling algorithms, such as Markov chain Monte Carlo (McMC) algorithms, are designed to sample the posterior distribution through sampling the high probable regions of the posterior probability distribution (Sen and Stoffa, 1996; Mosegaard and Sambridge, 2002). This leads to a thorough characterization of the possible solutions, and robust estimation of their uncertainties. Some case study applications of sampling-based McMC methods for petrophysical seismic inversion are presented (see, e.g., Grana 2018; de Figueiredo et al., (2019a, 2019b); Aleardi and Salusti, 2020).

The goal of this study is the characterization of a hard-rock carbonate reservoir through quantitative estimation of the porosity distribution as well as its uncertainty. We formulate the problem in a Bayesian framework and invert directly the seismic data to porosity using an McMC sampling-based approach via the Extended Metropolis-Hastings method (Mosegaard and Tarantola, 1995). In addition, we evaluate the feasibility of using a sampling-based approach to invert 3D seismic data probabilistically. The procedure followed in this work is twofold. Following the calibration of the Nur critical porosity model (Nur et al., 1998) and a semi-empirical inclusion-based model proposed by Keys and Xu (2002), we parametrize the inversion algorithm, i.e., the prior information, the data uncertainty (noise model), and the forward modeling operator.

In contrast to the routine practice of assuming uncorrelated white noise in probabilistic seismic inversion studies (Aleardi et al., 2018; Gunning and Sams, 2018; de Figueiredo et al., 2019a), we propose a proxy approach to take the inherent correlated nature of the band-limited seismic noise via a covariance matrix, in a probabilistic inversion of real seismic data.

In the following, we first present a geological overview of the case study. In the next section, the procedure of calibrating the rock-physics models is explained. Then, we outline the inversion methodology and associated parametrizations. Finally, we discuss the results of probabilistic inversion of the 2D and 3D real seismic data. This work provides a unique application of the probabilistic seismic inversion approach for this carbonate reservoir.

THE GEOLOGICAL SETTING

The study area is an oil field located in Southwest Iran. The target Sarvak formation is one of the most prolific reservoir zones in the Zagros area (Jooybari and Rezaie, 2016). This formation of middle Cretaceous age is about 600-m thick. It conformably overlies the Kazhdumi formation and disconformably underlies the Laffan formation (Figure 1). The Sarvak formation is generally described as a thick-bedded limestone interval with few dolomitic limestones and interbedded shale layers (Rahimpour-bonab et al., 2012.). Based on the reported biostratigraphy analyses, dolomite and shale are mainly concentrated in the upper part of the Sarvak formation, which is attributed to shallow marine Cenomanian-Turonian carbonates characterized by better reservoir quality and significant hydrocarbon contents. The Sarvak carbonates are subdivided into two major stratigraphical units namely the upper and lower Sarvak in terms of facies characteristics, sedimentary environments, and lithology types. The upper Sarvak unit with 400 m average thickness is characterized by bioclastic carbonates and significant reservoir quality, which comprises the major hydrocarbon-bearing zone. The diagenetic processes, facies analysis, sequence stratigraphy, and geological interpretation of the Sarvak formation have been extensively studied based on the petrophysical data, surface sections, and seismic interpretations (Assadi et al., 2016; Mehrabi et al., 2020). Based on the sequence stratigraphy studies, the upper Sarvak reservoir is divided into thirteen subzones

(Sar-1, 2, ..., 12, Sar-Intra). The average porosity, permeability, and net-to-gross ratio in the reservoir vary between high (Sar-3, 8, 12), moderate (Sar-4, 5), and poor quality (Sar-1, 6, 7, 9, 10, 11, Intra) and nonreservoir (Sar-2) subzones. In Figure 2, we present the 2D seismic profile used in this study superimposed by the well locations, their distance, their associated well-to-seismic ties, the tops of the reservoir subzones, as well as the horizons' TWT of four reservoir subzones (Sar-1, 3, 8, and Intra).

ROCK-PHYSICS MODELING

A data-driven rock-physics template is still a challenging issue for carbonate reservoirs due to the presence of a variety of pore types and microstructures, which could have a pronounced effect on the elastic properties of this rock type (Xu and Payne, 2009; Zhao et al., 2013). In this study, following the method proposed by Amini (2018) we calibrate the empirical model by Nur et al. (1998), and the semi-empirical inclusion-based model by Keys and Xu (2002) (Appendix A for more details). The carbonate formation in our case study dominantly comprises calcite minerals with low interbedded clay content. In this approach, we optimize the minerals' elastic moduli and density as well as the fitting parameters of the dry rock frame models – critical porosity and aspect ratio, simultaneously over four well data. This optimization approach is based on minimizing the misfit between the observed and modeled elastic moduli and density logs. Figure 3 shows the misfit surfaces for a range of plausible combinations of the calcite and clay minerals' elastic moduli. In this figure, the optimized values for minerals' elastic moduli and density are demonstrated by filled white circles. The variable critical porosity and pore aspect ratio estimated by this algorithm could potentially be used to assess the diagenetic evolution, pore-network structure, and elastic properties of the reservoir in conjunction with core and thin sections analysis (Fournier and Borgomano, 2009; Ruiz and Dvorkin, 2010). Figures 3c and 3f describe the cross plots of the optimized critical porosity and pore aspect ratio against the porosity. Table 1 represents the optimized minerals' elastic moduli and density as well as the regression coefficients (a1-a5) for critical porosity and pore aspect ratio as functions of porosity for the Nur and Keys-Xu models.

Figures 4 and 5 represent the results of calibration of the Nur model and Keys-Xu model over four wells, respectively. The results show that once calibrated, both rock-physics models could model the observed elastic moduli logs reasonably well. Heidari et al. (2020) propose both stochastic optimization and probabilistic approaches to present a rock-physics template for this carbonate reservoir. They argue that considering a constant critical porosity and pore aspect ratio for the whole reservoir zone, may lead to erroneous results in some reservoir intervals such as Sar-9, while here the results show that variable fitting parameters are more geologically realistic and improve the match between the observed and modeled elastic logs. However, as Figure 5 shows, the algorithm fails to capture the shear elastic moduli in well W06n. This reveals that describing the rock frame elastic moduli using the Keys-Xu model and a single fitting parameter (pore aspect ratio) may not be an appropriate choice for log data at this borehole. In addition, comparing Figures 3c and 3f, it is noted that the aspect ratio from the Keys-Xu model shows a larger scatter than the critical porosity from the Nur model. Therefore, the Nur model seems to be better than the Keys-Xu model for the dry rock-frame description of the reservoir. Although the literature suggests that calibration of rock-physics models for hard-rock carbonates is more challenging than clastic reservoirs due to the presence of complex pore types, microstructures, and heterogeneities (Eberli et al., 2003; Verwer et al., 2008; Fournier et al., 2018), our results show that a simple critical porosity model could model the observed saturated elastic moduli in this carbonate reservoir reasonably well. The dominant pore types in the Sarvak reservoir are intergranular macropores, intragranular dissolution pores, matrix dissolution pores, and microcracks, and aspect ratios could potentially be linked to the pore types (Xu and Payne, 2009). Additionally, the Sarvak reservoir is almost a pure carbonate reservoir with interbedded thin shale layers, but we do not consider the shale volume variations in the rock-physics model embedded in the inversion. This could inevitably lead to erroneous porosity estimation as the inversion overestimates the porosity value to compensate for the effect of shale in the shale bearing intervals.

WELL-TO-SEISMIC TIES

The carbonate platform is covered with 3D seismic data, which has been processed and stacked to near, middle, and far angle cubes. We use the middle angle stack for this study as the signal-to-noise ratio is usually higher for middle angle stacks. Figure 6 shows the region that is chosen for the 3D inversion, as well as the 2D line that passes through the four wells. At each well location, the compressional and shear sonic logs, the density log as well as the petrophysical logs (porosity, the volume of shale, water saturation, and gamma-ray) are available. We extract a statistical wavelet from the middle angle stack seismic data with a dominant frequency of 24 Hz (Figure 7).

One of the important steps before the seismic data inversion is the well-to-seismic tie. This procedure requires comparing the synthetic seismic trace and the observed seismic trace at the borehole. Using the available information of vertical seismic profile with check shots, we tie four wells to the observed seismic traces to obtain the wavelet scaler to be used in the seismic inversion. We superimpose the results of the well ties on the seismic section in Figure 2 next to each well. Although the well-to-seismic tie results are imperfect in some zones, the overall consistency between the synthetic and observed seismic traces as well as the available horizons' TWT (black dashed lines in Figure 2) for the subzones (Sar-1, 3, 8, and Intra) confirms the accuracy of the well tie procedure.

In addition to wavelet scaling, well-ties are also informative about the phase, signal-to-noise ratio, and how the geological details are upscaled to seismic bandwidth. The extracted wavelet from real data is zero-phase, which is used for synthetic seismic modeling and matches the observed seismic reasonably well. This indicates that the phase of the observed seismic data is close to zero. Figure 8 shows the petrophysical and sonic log data as well as the results of the well-to-seismic tie for well W08.

THEORY

Suppose $\mathbf{m}$ represents some model parameters describing physical properties (i.e., porosity in our study), and $\mathbf{d}$ refers to the noise-free physical response of the model $\mathbf{m}$ through the forward operator $\mathbf{d} = g(\mathbf{m})$. The observed data $\mathbf{d}_{\text{obs}}$ can be described by the following equation:

$$\mathbf{d}_{\text{obs}} = g(\mathbf{m}) + \mathbf{e} = \mathbf{d} + \mathbf{e}, \tag{1}$$

where $\mathbf{e}$ describes the noise, due to both the measurement and theoretical (modeling) errors (Tarantola, 2005). The inverse problem then consists of inferring information about the model parameters, given information about the observed data, forward operator, and noise model. In this study, we consider the probabilistic approach to solve the inverse problem.

The probabilistic inverse problem

Tarantola and Valette (1982) propose a probabilistic approach to solve the inverse problem, in which all information is quantified through a probability distribution or a likelihood function. In other words, the available information comprises the prior knowledge of the model parameters, as well as observed data. In the formulation of the inverse problem, we refer to the probability distribution of the model prior information as $\rho(\mathbf{m})$, which can come from any sources independent of the observed data, such as previous surveys, geoscientists knowledge, outcrops, and so forth. In this study, we use the porosity logs at four boreholes as the prior information. The geophysical data information is quantified through the likelihood function L, a probability distribution that quantifies the expected data residual for the model $\mathbf{m}$ as $L(\mathbf{m}) = f\left(\mathbf{d}_{obs} - \mathbf{g}(\mathbf{m})\right)$. Once the available information is quantified, the combined state of information, prior distribution, and the likelihood is obtained using the concept of *conjunction* *of states of information* (Tarantola and Valette, 1982). This leads to the solution of the inverse problem as the posterior probability distribution:

$$\sigma(\mathbf{m}) = \kappa\rho(\mathbf{m})L(\mathbf{m}), \tag{2}$$

where

$$\kappa^{-1} = \int \rho(\mathbf{m})L(\mathbf{m})d\mathbf{m} \tag{3}$$

is a normalization constant, which ensures that $\int \sigma(\mathbf{m})d\mathbf{m} = 1$.

Assuming a Gaussian distribution for the data uncertainty, the likelihood function is also Gaussian and is represented as (Mosegaard and Tarantola, 2002):

$$L(\mathbf{m}) = \left((2\pi)^{\mathrm{N}}\left|\mathbf{C}_D\right|\right)^{-\frac{1}{2}} exp\left(-\frac{1}{2}\left(\mathbf{d}_{obs} - \mathbf{g}(\mathbf{m})\right)^T \mathbf{C}_D^{-1}\left(\mathbf{d}_{obs} - \mathbf{g}(\mathbf{m})\right)\right), \tag{4}$$

where N is length of data and $\mathbf{C}_D$ is the data covariance, which can be split into contributions from the measurement errors $\mathbf{C}_{\mathrm{d}}$ and modeling error $\mathbf{C}_{\mathbf{t}}$ as $\mathbf{C}_{\mathrm{D}} = \mathbf{C}_{\mathrm{d}} + \mathbf{C}_{\mathbf{t}}$, assuming independence of the two (Tarantola, 2005).

Sampling the posterior probability distribution

To solve the probabilistic inverse problem, it is necessary to describe the posterior distribution $\sigma(\mathbf{m})$ either analytically, or numerically. An analytical description of the posterior distribution is typically only possible for linear Gaussian inverse problems (Tarantola and Valette, 1982). For nonlinear inverse problems, sampling methods can be utilized instead to generate a sample (a collection of model realizations) distributed according to $\sigma(\mathbf{m})$. The statistical analyses of the posterior distribution give an extensive insight into the model parameter and its uncertainty. McMC methods based on variants of the Metropolis and Metropolis-Hastings algorithms (Metropolis et al., 1953; Hastings, 1970), are among the most widely used algorithms to sample from $\sigma(\mathbf{m})$. In this study, we use the extended Metropolis-Hastings algorithm (Mosegaard and Tarantola, 1995), through the SIPPI toolbox developed by Hansen et al. (2013) to sample the posterior distribution. In contrast to the classic Metropolis-Hastings algorithm, using the extended Metropolis-Hastings algorithm, neither needs to evaluate the posterior probability distribution $\sigma(\mathbf{m})$, nor the prior probability distribution of a given model $\mathbf{m}$. There are only two conditions, which should be satisfied to apply the extended Metropolis algorithm. The first requirement is the evaluation of the likelihood function in equation (4), which is most often straightforward, as it requires solving the forward problem and assessing the corresponding data fit given the noise model. Secondly, one must be able to perform a random walk in the space of the prior acceptable models to sample $\rho(\mathbf{m})$ (Mosegaard and Tarantola, 1995). We make use of the sequential Gibbs sampling algorithm, to perform a random walk in the prior probability space, as it provides the ability to sample complex prior distributions (Hansen et al., 2012).

To run the extended Metropolis-Hastings algorithm, we should define at least three main components, i.e., the prior model, the solution of the forward problem, as well as the data uncertainty (noise model).

Prior model

We assume a multivariate Gaussian distribution for the prior model, which is specified by a mean vector/scalar $\mathbf{m}_0$ and an isotropic covariance model $\mathbf{C}_\mathbf{m}$. To obtain the covariance matrix, it is necessary to estimate the spatial dependency of the porosity in each well location. In geostatistical approaches, the spatial dependency of the variables as a function of lag is estimated by an experimental semi-variogram (Isaaks and Srivastava, 1989). In the geostatistical modeling procedure, we aim to find out which variogram model and which parameters (i.e., sill, nugget, and range) best represent the spatial trends in the experimental variogram. Therefore, for prior model parameterization, i.e., accounting for its covariance and the mean, we first calculate the experimental semi-variogram of the four porosity logs and their mean. Then, we obtain the theoretical semi-variogram model, which best represents the mean of the four experimental semi-variograms. We assume the average of the variances of the four logs as the sill of the fitted theoretical semi-variogram (Figure 9). Finally, based on the relation between the semi-variogram configuration and the covariance matrix, we estimate the Gaussian covariance matrix $\mathbf{C}_{\mathbf{m}}$ of the prior model (see, e.g., Goovaerts, 1997). We calculate the mean of the porosity of the four wells and assign it to the constant mean of the prior model $\mathbf{m}_0$. To represent the prior model numerically, we use the fast Fourier transform moving average (FFT-MA) method proposed by Le Ravalec et al. (2002), an efficient approach for generating the independent realizations from a stationary multivariate Gaussian realization. Also, we apply the inverse normal score transform (see, e.g., Goovaerts, 1997) to ensure that the distribution of the model realizations follows the target distribution (Hansen et al., 2013). It should be noted that since the Gaussian distributions are defined in the entire set of real numbers, we define a realistic range to avoid the porosity values fall outside the physical range.

Forward model

To solve the forward modeling problem and generate the synthetic trace associated with each model parameter, we use the widely popular one-dimensional convolution approach (Yilmaz, 2001). Figure 10 outlines the main components of this procedure. The peterophysical logs, i.e., the volume of shale and water saturation, as well as the porosity realization are converted to elastic parameters using RPM. To generate the middle angle-stack seismic response, considering the corresponding range of angle of incidence (15-23 degrees), we use the Zoeppritz equations (Aki and Richards, 1980) to compute the PP reflectivity coefficients from the model parameters. Finally, we convolve the extracted statistical wavelet with the average reflectivity series to generate the corresponding synthetic trace.

Noise model

The noise model should ideally include information about the measurement errors as well as modeling errors (Tarantola, 2005). However, in real data applications, the description of the noise and distinction between the above-mentioned noise sources is not trivial (Madsen et al., 2017). Among few publications on this subject, Jakobsen and Hansen (2019) explore the effect of correlated and uncorrelated noise in a direct Bayesian inversion of 1D synthetic seismic data to lithofacies. They show that considering correlated noise improved the resolution of the model parameters compared to the case of the white uncorrelated noise model. Madsen et al. (2017) also adopt a hierarchical Bayesian approach to infer the properties of the noise model as a part of inversion. In this study, we assume that the forward modeling, as well as the model parametrizations are exact, and the data uncertainty is just attributed to the measurement errors. Due to the band-limited nature of the seismic data, it contains vertically correlated noise, where the noise samples are vertically coupled along the TWT axis. However, in probabilistic seismic data inversion, it is a common practice to assume an uncorrelated white noise, where the noise covariance matrix in equation (4) is described by the noise variance σ^2 and the identity matrix $\mathbf{I}$ in the form of $\mathbf{C}_d = \sigma^2\mathbf{I}$. Finding a representative geometry for the covariance matrix is a key aspect of a correlated noise setup. Due to the effective processing of the seismic data, uncorrelated (white) noises are filtered out. Therefore, the remainder of the noise in the seismic data is correlated (colored) with the bandwidth in the range of the bandwidth of the seismic data (wavelet).

Here, to simulate the realistic correlated noise and address the correlation of the noise samples, we generate 531 realizations of a Gaussian random reflectivity $\mathcal{N}(0,0.0324)$ with the length of 281 samples and convolve them with the estimated seismic wavelet. Figures 11a and b show the 2D band-limited Gaussian noise realizations and their corresponding covariance matrix. The mean of the nonzero diagonals of the covariance matrix, the seismic wavelet as well as their corresponding frequency spectrum is shown in Figures 11c and d, respectively. Regarding these figures, the mean of the nonzero diagonals of the covariance matrix could be a reasonable approximation of the seismic wavelet, as their main lobes are almost similar and their frequency spectrums are approximately in the same range. Therefore, we presume that the seismic wavelet is a suitable proxy for capturing the coupling of data samples for both signal and noise within the seismic bandwidth. Consequently, in contrast to the routine practice where the main diagonal of the noise covariance matrix is a delta function, we insert the seismic wavelet along the main diagonal of the covariance matrix to account for the correlation of the noise samples more realistically. To evaluate this assumption, we construct a synthetic seismic trace (Figure 12a) using a porosity realization from a multivariate Gaussian distribution prior model, in conjunction with the Nur rock-physics model and the forward modeling procedure. Then, we add a correlated (band-limited) Gaussian noise (Figure 12b) to the noise-free seismic trace to generate a noisy seismic trace (Figure 12c). We account for correlated noise in one case (A) and uncorrelated noise in another case (B) in probabilistic inversion. Also, we set the iteration of the sampling algorithm such that the algorithm can sample the full posterior distribution within a reasonable time. The porosity realizations for both these assumptions are shown in Figure 12d and Figure 12e, respectively. Comparing the results of these both cases indicates that, accounting for the uncorrelated noise in inversion, where the noise in the data is correlated, leads to apparently well-resolved features with lower uncertainty. In addition, assuming uncorrelated noise leads to a harder sampling due to the inability of the algorithm to reach the burn-in phase and the data is overfitted through an optimization procedure rather than a sampling procedure.

As the estimation of the noise magnitude and noise shape for real data applications is not trivial, care should be taken in accounting for the noise model. In this study, for inversion of the real seismic data, we account for the correlated noise as mentioned above, where the noise magnitude (SNR = 3.3) is estimated roughly from the well-to-seismic tie residuals.

RESULTS AND DISCUSSION

We evaluate the inversion performance by analyzing the porosity posterior realizations for both the seismic section along with the wells and the traces at well locations. The results of the inversion using both the Nur and Keys-Xu rock-physics models are shown in Figures 13 and 14, respectively. The seismic section superimposed by the well-to-seismic tie results as well as the horizons' TWT of Sar-1, 3, 8, and Intra subzones are shown in Figures 13a and 14a. Figures 13b and 14b show the pointwise porosity posterior mean along the profile superimposed by the porosity values at well locations. We resample the porosity logs to the seismic scale to ensure the consistency of the sampling interval, i.e., 1 ms. These figures suggest that the inversion could resolve some thin layers reasonably well, flagged by white arrows. In addition, some features on the seismic section (Figures 13a and 14a) related to the geological disconformities are successfully resolved by the porosity posterior mean shown by black ellipses. In addition, the distortion on the seismic section, flagged by black arrows close to the well W04n is detectable on the porosity posterior mean section. Comparison of the mean posterior model and the observed porosity logs at well locations indicates that the inversion can resolve the true porosity reasonably well. The pointwise standard deviation of the porosity posterior realizations is shown in Figures 13c and 14c, which quantify the uncertainty of the porosity values. The variability of this quantity represents the capability of the algorithm to generate enough independent realizations of the porosity, leading to better uncertainty assessment. Using the optimized regression coefficients obtained through the rock-physics calibration procedure (Table 1), we convert the mean porosity model by the Nur and Keys-Xu rock-physics models to critical porosity and pore aspect ratio, respectively. These properties are shown in Figures 13d and 14d, respectively. In contrast to the porosity posterior mean, the variations of the critical porosity, as well as the pore aspect ratio are more pronounced. For example, the low porosity region in Figures 13b and 14b is characterized on its associated critical porosity and pore aspect ratio sections by resolved thin layers with variable critical porosity and pore aspect ratio (see white ellipses on Figures 13b, d and Figures 14b, d). Comparison of the pointwise critical porosity and the pore aspect ratio in Figures 13d and 14d indicates the positive correlation of these two properties, which follows the Keys-Xu (2002) argument on the critical porosity and pore aspect ratio correlation, as the increase of the critical porosity leads to increase of the pore aspect ratio.

To better evaluate the porosity posterior realizations, we obtain the probability values of the posterior mean for two facies defined via porosity cut-offs. Figures 13e, f, and 14e, f depict the probability values associated with facies-1 with the porosity between zero and 0.15 and facies-2 with the porosity between 0.15 and 0.3, respectively. These probability sections facilitate the interpretation of the posterior mean model as they indicate the uncertainty associated with the inverted porosities. In addition, the interpreter can easily flag the regions where the porosity values are in the desired range. Comparison of the results obtained by utilizing both rock-physics models shows no tangible difference and they both characterize the reservoir property and its uncertainty equally well.

The statistics of the porosity posterior realizations, i.e., their mean (white), a 95% confidence interval (CI, pink dashed lines), and the observed porosity (black) are shown for four well logs in Figure 15b (for Nur model) and 15c (for Keys-Xu model). The porosity realizations are depicted as the density plots, where the background colors represent the probability of the realizations at each time sample. The posterior mean model shows a reasonable match to the measured porosity for all four well logs, except in zones flagged by white arrows. The statistical analysis indicates that around 95%, 90%, and 81% of the true porosity are found in a 95% CI for wells W04n, W08, and W10 using the Nur model. These values are about 91%, 89%, and 88% for the Keys-Xu model. The mismatch between the predicted and observed porosity model is more notable for well W06n as only 73% of the true porosities are found in a 95% CI using both rock-physics models. The inconsistency between the modeled and observed porosity can be attributed to the issues of the seismic resolution, the uncertainty related to rock-physics modeling due to the presence of the thin interbedded shaly layers, or the imperfect well-to-seismic ties. For well W06n, the effect of rock-physics and well-tie imperfections are more pronounced, especially for the Keys-Xu model as it fails to calibrate the observed elastic moduli properly (see Figure 5). The petrophysical analyses of our case study characterize a low porosity cap rock in Sar2 as a nonreservoir zone. The shaly zones of four wells are marked with brown in Figure 15. The inversion fails to resolve the true porosity values of these zones for all the wells and overestimates the porosity. This imperfection is attributed to the presence of shale, where the clay content poses uncertainty to the inversion results, as the RPM embedded in the inversion does not include the shale volume variations. In addition, the inversion fails to capture the trend of the true porosity even in the relatively thicker Sar-12 subzone in wells W06n, W08, and W10. This subzone was reported as a pure calcite zone and the accuracy of well-to-seismic-ties is acceptable, therefore, the observed inconsistency in this subzone can be attributed to the presence of the layers thinner than the seismic resolution. Figure 16 shows the 1D marginal distributions of the porosity realizations at well locations compared with the histogram of the porosity well logs for both rock-physics models. It is obvious that except for well W06n, the marginal distributions of the porosity realizations for the other three wells are consistent with the histogram of the porosity logs, which confirms the performance of the inversion as well as the accuracy of the prior and the noise model for this real data.

Comparison with the 2D geological model

We also evaluate the consistency of the existing geological model through a geomodel-to-seismic modeling workflow as well as a direct comparison of the inverted porosity with the porosity in the geological model. The geological model has been constructed using the available well logs through a sequential Gaussian simulation approach, where deterministic seismic inversion products were used as lateral constrains. The client has provided us both the geological model and the deterministic inversion results. Our geomodel-to-seismic modeling workflow includes the estimation of the elastic properties in the geological model by application of the calibrated rock-physics models, followed by convolution of the reflectivity series with the extracted wavelet. We align the TWT associated with the geological model (Figure 17 a) and its associated synthetic seismic (Figure 17 c) to the observed seismic data (Figure 17 d) using a horizon pair in TWT and depth. The estimated velocity from the rock-physics model governs the interval TWT between the top and base of the reservoir. This allows us to use the relative TWT location of the synthetic and observed seismic events – in addition to amplitude information – as a metric for assessing the consistency of the geological model with the seismic data. Comparison of the horizons' TWT of Sar-1, Sar-3, Sar-8, and Sar-Intra subzones, shown by dashed lines and white arrows, with the top and base of the reservoir in the geological model represents that TWT thickness of the reservoir in the geological model is higher than the observed TWT thickness. This means that the porosity values provided by the geostatistical modeling have been overestimated.

Figure 17b shows the mean porosity model obtained by the probabilistic inversion algorithm. The reconstructed seismic section of the mean porosity model is shown in Figure 17e. At first glance, the higher frequency content of the geological model is notable. This is because this model is built at the resolution of the well log data. However, this is not enough to make it superior to the porosity model obtained through probabilistic seismic inversion. According to the available reports provided by the client, some geological features such as two faults F-1 and F-2 have been added to the structure of the geological model. These two faults are resolved with the same structure on the synthetic seismic response. The inversion could resolve some thin layers reasonably well, as they are notable in both the geological model and the mean porosity model such as the layers A-1, A-2 (flagged by black arrows), and A-3 (flagged by a black ellipse). However, the high porosity thin layers such as B-1 and B-2 are not resolved in the mean porosity model, as the resolution of the mean of the realizations is lower than the resolution of individual realizations. The geological model shows a high porosity continuous region between the wells W04n and W10 (the black ellipse C), whereas this region is localized around the well W10 in the mean porosity model. There is also a wide low porosity region (the black ellipse D) on the geological model, which is terminated by a high porosity zone, while this region is characterized as a continuous low porosity region in the mean porosity model. The seismic response of this feature is a doublet on the reconstructed seismic data by the mean porosity model, whereas this doublet is not detectable on the synthetic seismic data corresponding to the geological model. The seismic responses of the feature A-3 from both the geological model and mean porosity model are flagged in Figures 17c and d. It is obvious that the seismic response of this feature from the mean porosity model is tangible and consistent with the observed seismic response, as the seismic amplitudes variations are consistent with the porosity variations. However, this feature is not detectable on the seismic response of the geological model.

Figure 18 demonstrates the porosity models estimated through the geostatistical approach (Figure 18a), the two-step deterministic seismic inversion (Figure 18b), and the single-step probabilistic seismic inversion (Figure 18c). The model provided by the deterministic seismic inversion is smooth, as it could not resolve the thin layers and other geological features precisely. However, as this model was used as the lateral constraint in the geological model generation through the geostatistical approach, there are some features in this model such as H-1 and H-2, which are consistent with the geological model.

These evaluations represent that the porosity model obtained through the single-step probabilistic seismic inversion shows a reasonable consistency with geological model, and it is much trustworthy as it could reconstruct the observed seismic data reasonably well.

Application to the 3D seismic data

We show the results of inverting the 3D seismic cube from the specified region in Figure 6 as time maps in Figures 19 and 20. The Nur rock-physics model is used in this 3D seismic inversion application. Figure 19 shows the map of the seismic amplitudes, the porosity posterior mean model, as well as the standard deviation of the porosity realizations across the Sar-1, 3, 8, and Intra subzones. Figure 20 describes the map of the critical porosity as well as the probability maps of facies-1 and facies-2. The variability of the porosity distribution in Sar-3 and Intra subzones is more tangible compared to Sar-1 and 8 subzones, where most of the porosity values are less than 0.1. However, there is an area close to well W08 in Sar-3 subzone, which shows the high-quality reservoir potential. These maps also show a low porosity and low critical porosity zone in the west and southwest part of the studied region for the Sar-1 subzone. The center, east, and southeast of the region are characterized as a potentially high-quality reservoir in the Sar-3 subzone. While these high-quality regions are distributed in the whole Sar-Intra subzone, especially from the center to the north, these regions are also characterized by the probability of the porosity cut-offs (facies) in Figure 20c, as the probability of high porosity distribution in these regions is high. The values of the standard deviation maps, especially close to the wells indicate the high precision of the estimated porosity in these reservoir subzones. Comparing the critical porosity maps in Figure 20a in conjunction with thin sections or other laboratory measurements or interpretation maps could give a better insight to acknowledge the variation of the diagenetic procedures in these subzones. For example, the variations of the critical porosity distribution of Sar-1and Sar-8 subzones are more notable than Sar-3 and Sar-Intra subzones, which could be attributed to the complexity of the pore structures in Sar-1 and Sar-8 subzones. The probability of the facies distributions shown in Figures 20b and c confirms that Sar-3 and Sar-Intra subzones are of higher quality reservoirs than Sar-1 and Sar-8 subzones. Regarding these probability maps, the regions with the porosity higher than 0.15 are dominant in Sar-3 and Sar-Intra subzones, particularly in the areas closer to the well W04n, and W10. Sar-8 subzone shows high probability facies with porosity higher than 0.15 near well W08. Analyzing the percentiles is another approach to analyze the uncertainty of the model parameters distribution. To provide another visual depiction of the porosity realizations, we show the 5th, 25th, 75th, and 95th percentiles of the porosity realizations for the reservoir subzones in Figures 21 and 22, respectively. These figures provide a good insight into the uncertainty assessment of the porosity distributions for the reservoir subzones. In addition, this quantitative uncertainty evaluation could facilitate the interpretation of the reservoir porosity distribution for further decision making and well planning for this reservoir.

CONCLUSIONS

The results in this study indicate that the proposed sampling-based probabilistic inversion approach can be successfully used to invert the large-scale 3D seismic data directly to porosity. The results of 3D seismic data inversion give a good insight into the quality of different reservoir subzones. The results also indicate that the seismic wavelet is a good proxy for taking the inherent correlated nature of the band-limited seismic noise into account via a covariance matrix. The utilized single-step probabilistic inversion approach could properly characterize the porosity distribution and the associated uncertainty for the Sarvak reservoir. It could also resolve some thin layers as well as some geological features compared to the geological model obtained by the geostatistical simulation. The geomodel-to-seismic modeling of the geological model indicate that the constructed seismic data from this model is not consistent with the observed data. On the other hand, the porosity model obtained by the probabilistic inversion could reasonably reconstruct the observed seismic data. In addition, comparing the TWT thickness of the base of the reservoir in the synthetic seismic data from the geological model and the observed seismic data indicate that the porosity in the geological model is overestimated and needs further updates. Using both the Nur and Keys-Xu rock-physics models as a part of the forward modeling operator provides porosity models that describe the reservoir properties equally well. Therefore, providing that calibrated properly, both of these simple rock-physics models with a single fitting parameter can be representative of the dry rock elastic moduli in this carbonate reservoir. The statistical analyses of the porosity posterior realization at well locations show a high consistency between the inversion results and the observed porosity logs, except for the shaly zones as well as the regions with a poor well-to-seismic tie. The distribution of the porosity and the associated uncertainty, the critical porosity, as well as pore aspect ratio can potentially be used in conjunction with the laboratory data obtained by analyzing the thin sections and core samples to improve the interpretation of this reservoir and better decision making for further field developments.

APPENDIX A

ROCK-PHYSICS MODEL PARAMETERS

The Gassmann fluid substitution model (equations (A-1) and (A-2)) is the key building block of the rock-physics calibration workflow. The empirical Nur critical porosity model (equation (A-3)), as well as the semi-empirical inclusion-based Keys-Xu model (equation (A-4)), are used for estimation of the rock frame bulk and shear elastic moduli (K_{frame}, G_{frame}). The mean of the Hashin-Shtrikman upper and lower bounds (Hashin and Shtrikman, 1963) are used to calculate the minerals' effective bulk and shear moduli (K_0, G_0).

$$K_{sat} = K_{frame} + \frac{\left(1 - {K_{frame}}/{K_0}\right)^2}{{\phi}/{K_{fluid}} + {1-\phi}/{K_0} - {K_{frame}}/{K_0^2}}, \qquad \text{A-1}$$

$$G_{sat} = G_{frame}, \qquad \text{A-2}$$

$$\begin{aligned} K_{frame} &= K_0\left(1 - {\phi}/{\phi_c}\right) \\ G_{frame} &= G_0\left(1 - {\phi}/{\phi_c}\right) \end{aligned}, \qquad \text{A-3}$$

$$\begin{aligned} K_{frame} &= K_0\left(1-\phi\right)^{P(\alpha)} \\ G_{frame} &= G_0\left(1-\phi\right)^{Q(\alpha)} \end{aligned}, \qquad \text{A-4}$$

where K_{sat} and G_{sat} are the saturated bulk and shear moduli, K_{fluid} is the effective bulk modulus of the fluid mixture using harmonic averaging of the in-situ oil and brine bulk moduli (Wood, 1955), which are calculated using pressure-volume-temperature (PVT) data (not shown here) and the empirical equations by Batzle and Wang (1992). ϕ and ϕ_c are the effective porosity and critical porosity, respectively. In equation A-4, P and Q are the pore shape factors related to the pore aspect ratio α (Mavko et al., 2009).

REFERENCES

Abdollahie Fard, I., A. Braathen, M. Mokhtari, and A. Alavi, 2006, Interaction of the Zagros Fold–Thrust Belt and the Arabian-type, deep-seated folds in the Abadan Plain and the Dezful Embayment, SW Iran: Petroleum Geosciences, **12**, no. 4, 347-362.

Aki, K. and P. Richards, 1980, Quantitative Seismology: Theory and Methods: W. H. Freeman and Co.

Amini, H, 2018, Calibration of minerals' and dry rock elastic moduli in sand-shale mixtures: 80th EAGE Conference and Exhibition, Expanded Abstracts, 1-5.

Aleardi, M, 2018, Applying a probabilistic seismic-petrophysical inversion and two different rock physics models for reservoir characterization in offshore Nile Delta: Journal of Applied Geophysics, **148**, 272–286.

Aleardi, M., F. Ciabarri, and T. Gukov, 2018, A two-step inversion approach for seismic-reservoir characterization and a comparison with a single-loop Markov-chain Monte Carlo algorithm: Geophysics, **83**, no. 3, R227–R244.

Aleardi, M., and A. Salusti, 2020, Markov chain Monte Carlo algorithms for target-oriented and interval-oriented amplitude versus angle inversions with non-parametric priors and non-linear forward modellings: Geophysical Prospecting, **68**, no. 3, 735–760.

Assadi, A., J. Honarmand, S. A. Moallemi, and I. Abdollahie-Fard, 2016, Depositional environments and sequence stratigraphy of the Sarvak Formation in an oil field in the Abadan Plain, SW Iran: Facies, **62**, no. 4, 1-22.

Aster, R.C., B. Borchers, and C. H. Thurber, 2018, Parameter estimation and inverse problems: Elsevier.

Batzle, M., and Z. Wang, 1992, Seismic properties of pore fluids: Geophysics, **57**, 1396–1408.

Buland, A. and H. More, 2003, Bayesian linearized AVO inversion: Geophysics, **68**, no, 1, 185–198.

de Figueiredo, L.P., D. Grana, M. Roisenberg, and B. B. Rodrigue, 2019a, Gaussian mixture Markov chain Monte Carlo method for linear seismic inversion: Geophysics, **84**, 3, R463-R476.

de Figueiredo, L.P., D. Grana, M. Roisenberg, and B. B. Rodrigue, 2019b, Multimodal Markov chain Monte Carlo method for nonlinear petrophysical seismic inversion: Geophysics, **84**, no. 5, M1-M13.

Doyen, P., 2007, Seismic Reservoir Characterization: EAGE.

Eberli, G.P., G. T. Baechle, F. S. Anselmetti, and M. L. Incze, 2003., Factors controlling elastic properties in carbonate sediments and rocks: The Leading Edge, **22**, no. 7, 654-660.

Fjeldstad, T., and D. Grana, 2018, Joint probabilistic petrophysics-seismic inversion based on Gaussian mixture and Markov chain prior models: Geophysics, **83**, no. 1, R31-R42.

Fournier, F., M. Pellerin, Q. Villeneuve, T. Teillet, F. Hong, E. Poli, J. Borgomano, P. Léonide, and A. Hairabian, 2018, The equivalent pore aspect ratio as a tool for pore type prediction in carbonate reservoirs: AAPG Bulletin, **102**, no. 7, 1343-1377.

Fournier, F., and J. Borgomano, 2009, Critical porosity and elastic properties of microporous mixed carbonate-siliciclastic rocks: Geophysics, **74**, no. 2, E93-E109.

Goovaerts, P, 1997, Geostatistics for natural resources evaluation: Oxford University Press on Demand.

Goodway, B., T. Chen, and J. Downton, 1997, Improved AVO fluid detection and lithology discrimination using Lamé petrophysical parameters;"λρ","μρ", & "λ/μ fluid stack", from P and S inversions: SEG technical program, Expanded Abstracts, 183-186.

Grana, D., T. Fjeldstad, and H. More, 2017, Bayesian Gaussian Mixture Linear Inversion for Geophysical Inverse Problems: Mathematical Geosciences, **49**, no. 4, 493–515.

Grana, D. and E. Della Rossa, 2010, Probabilistic petrophysical-properties estimation integrating statistical rock physics with seismic inversion: Geophysics, **75**, no. 3, O21-O37.

Grana, D., 2016, Bayesian linearized rock-physics inversion: Geophysics, **81**, no. 6, D625-D641.

Grana, D., 2018, Joint facies and reservoir properties inversion: Geophysics, **83**, M15–M24.

Grana, D., 2020, Bayesian petroelastic inversion with multiple prior models: Geophysics, **85**, M57-M71.

Ghon, G., D. Grana, C. E. Rankey, G. T. Baechle, F. Bleibinhaus, X. Lang, P. L. de Figueiredo, and M. C. Poppelreiter, 2020, Bayesian facies inversion on a partially dolomitized isolated carbonate platform. A case study from Central Luconia province, Malaysia: Geophysics, **86**, B98-B108.

Gunning, J., and M. E. Glinsky, 2004, Delivery: An open-source model-based Bayesian seismic inversion program: Computers and Geosciences, **30**, no. 6, 619–636.

Gunning, J., and M. Sams, 2018, Joint facies and rock properties Bayesian amplitude-versus-offset inversion using Markov random fields: Geophysical Prospecting, **66**, no. 5, 904–919.

Hansen, T.M., K. S. Cordua, M. C. Looms, and K. Mosegaard, 2013, SIPPI: A Matlab toolbox for sampling the solution to inverse problems with complex prior information: Part 1—Methodology: Computers & Geosciences**, 52**, 470-480.

Hansen, T.M., K. S. Cordua, and K. Mosegaard, 2012, Inverse problems with non-trivial priors: efficient solution through sequential Gibbs sampling: Computational Geosciences, **16**, no. 3, 593-611.

Hashin, Z. and S. Shtrikman, 1963, A variational approach to the theory of the elastic behaviour of multiphase materials: Journal of the Mechanics and Physics of Solids, **11**, no. 2, 127-

140.

Hastings, W.K., 1970, Monte Carlo sampling methods using Markov chains and their applications: Biometrika, **57**, no. 1, 97.

Heidari, A., N. Amini, H. Amini, M. E. Niri, A. Zunino, and T. M. Hansen, 2020, Calibration of two rock-frame models using deterministic and probabilistic approaches: Application to a carbonate reservoir in south-west Iran: Journal of Petroleum Science and Engineering, **192**, 107266.

Isaaks, E. H., and R. M. Srivastava, 1989, An introduction to applied geostatistics: Oxford university press.

Jakobsen, A.F. and H. J. Hansen, 2019, Exploring Noise Models in Approximate Bayesian Inversion for Facies: 81th EAGE Conference and Exhibition, Extended Abstracts, 1-5.

Jooybari, A., and P. Rezaie, 2016, Petrophysical evaluation of the Sarvak formation based on well logs in Dezful Embayment, Zagros Fold Zone, south west of Iran: Engineering, Technology & Applied Science Research, **7**, no. 1, 1358-1362.

Keys, R.G., S. Xu, 2002, An approximation for the Xu-White velocity modelApproximation for the Xu-White Model: Geophysics, **67**, no. 5, 1406-1414.

Kolbjørnsen, O., A. Buland, R. Hauge, P. Røe , A. O. Ndingwan, E. Aker, 2020, Bayesian seismic inversion for stratigraphic horizon, lithology, and fluid prediction: Geophysics, **85**, no. 3, R207-R221.

Le Ravalec, M., B. Noetinger, and L. Y. Hu, 2000, The FFT moving average (FFT-MA) generator: An efficient numerical method for generating and conditioning Gaussian simulations: Mathematical Geology, **32**, no. 6, 701-723.

Malinverno, A., and V. A. Briggs, 2004, Expanded uncertainty quantification in inverse problems: Hierarchical Bayes and empirical Bayes: Geophysics, **69**, no. 4, 1005-1016.

Madsen, R. B., and T. M. Hansen, 2018, Estimation and accounting for the modeling error in probabilistic linearized amplitude variation with offset inversion: Geophysics, **83**, no. 2, N15–N30.

Madsen, R. B., A. Zunino, and T. M. Hansen, 2017, On inferring the noise in probabilistic seismic AVO inversion using hierarchical Bayes: SEG Annual Meeting proceedings, 601-605.

Mavko, G., T. Mukerji, and J. Dvorkin, 2009, The Rock Physics Handbook: Tools for Seismic Analysis of Porous Media: Cambridge University Press.

Mehrabi, H., B. Bagherpour, and J. Honarmand, 2020, Reservoir quality and micrite textures of microporous intervals in the Upper Cretaceous successions in the Zagros area, SW Iran: Journal of Petroleum Science and Engineering, **192**, 107292.

Metropolis, N., A. W., Rosenbluth, M. N. Rosenbluth, A. H. Teller, E. and Teller, 1953, Equation of state calculations by fast computing machines: The journal of chemical physics, **21**, no. 6, 1087-1092.

Mosegaard, K., and M. Sambridge, 2002, Monte Carlo analysis of inverse problems: Inverse problems, **18**, no. 3, R29.

Mosegaard, K., and A. Tarantola, 1995, Monte Carlo sampling of solutions to inverse problems*:* Journal of Geophysical Research: Solid Earth, **100**, no. B7, 12431-12447.

Mosegaard, K., and A. Tarantola, 2002, Probabilistic approach to inverse problems: International Geophysics Series, **81**, no. A, 237-268.

Nur, A., G. Mavko, J. Dvorkin, and D. Galmudi, 1998, Critical porosity: A key to relating physical properties to porosity in rocks: The Leading Edge, **17**, no. 3, 357-362.

Rahimpour-Bonab, H., H. Mehrabi, A. Navidtalab, and E. Izadi-Mazidi, 2012, Flow unit distribution and reservoir modelling in cretaceous carbonates of the Sarvak Formation, Abteymour Oilfield, Dezful Embayment, SW Iran: Journal of Petroleum Geology, **35**, no. 3, 213-236.

Rimstad, K., P. Avseth, and H. More, 2012, Hierarchical bayesian lithology/fluid prediction: A north sea case study: Geophysics, **77**, no. 2, B69-B85.

Ruiz, F. and J. Dvorkin, 2010, Predicting elasticity in nonclastic rocks with a differential effective medium model: Geophysics, **75**, no. 1, E41-E53.

Sajeva, A., M. Aleardi, and A. Mazzotti, 2017, Genetic algorithm full-waveform inversion: Uncertainty estimation and validation of the results: Bollettino di Geofisica Teorica ed Applicata, **58**, no. 4, 395–414.

Sen, M. K., and P. L. Stoffa, 1996, Bayesian inference, Gibbs' sampler and uncertainty estimation in geophysical inversion: Geophysical Prospecting, **44**, no. 2, 313–350.

Talarico, S.e.C.E., D. Grana, P. L. de Figueiredo, 2020, Uncertainty quantification in seismic facies inversion: Geophysics, **85**, M43-M56.

Tarantola, A. and B. Valette, 1982, Inverse problems= quest for information: Journal of Geophysics, **50**, no. 1, 159–170.

Tarantola, A., 2005, Inverse problem theory and methods for model parameter estimation: Society for Industrial and Applied Mathematics.

Verwer, K., H. Braaksma, and J. A. Kenter, 2008, Acoustic properties of carbonates: Effects of rock texture and implications for fluid substitution: Geophysics, **73**, no. 2, B51-B65.

Wood, A.B., 1955, A Textbook of Sound: The McMillan Co, New York.

Xu, S., and M. A. Payne, 2009, Modeling elastic properties in carbonate rocks: The Leading Edge, **28**, no. 1, 66-74.

Yilmaz, Ö. Z., 2001, Seismic Data Analysis: Processing, Inversion, and Interpretation of Seismic Data: Society of Exploration Geophysicists.

Zhao, L., M. Nasser, and D. H. Han, 2013, Quantitative geophysical pore-type characterization and its geological implication in carbonate reservoirs: Geophysical Prospecting, **61**, no. 4, 827-841.

TABLES

Table 1. Calibrated rock properties using the Nur and Keys-Xu models.

Model	Bulk Modulus (GPa)		Shear Modulus (GPa)		Density (gr/cm3)		$\phi_c = \mathbf{a}_1 + \mathbf{a}_2\phi$, $\phi < \mathbf{a}_5$, $\phi_c = \mathbf{a}_3 + \mathbf{a}_4\phi$, $\phi > \mathbf{a}_5$ $\alpha = \mathbf{a}_1 + \mathbf{a}_2\phi$, $\phi < \mathbf{a}_5$, $\alpha = \mathbf{a}_3 + \mathbf{a}_4\phi$, $\phi > \mathbf{a}_5$
	Calcite	Clay	Calcite	Clay	Calcite	Clay	$\mathbf{a}_{1-5}$
Nur	66	20	30	5	2.74	2.23	0.05, 1.73, 0.21, 0.46, 0.12
Keys-Xu	68	18	20	9	2.74	2.23	0.01, 1.23, 0.17, 0.65, 0.12

FIGURES

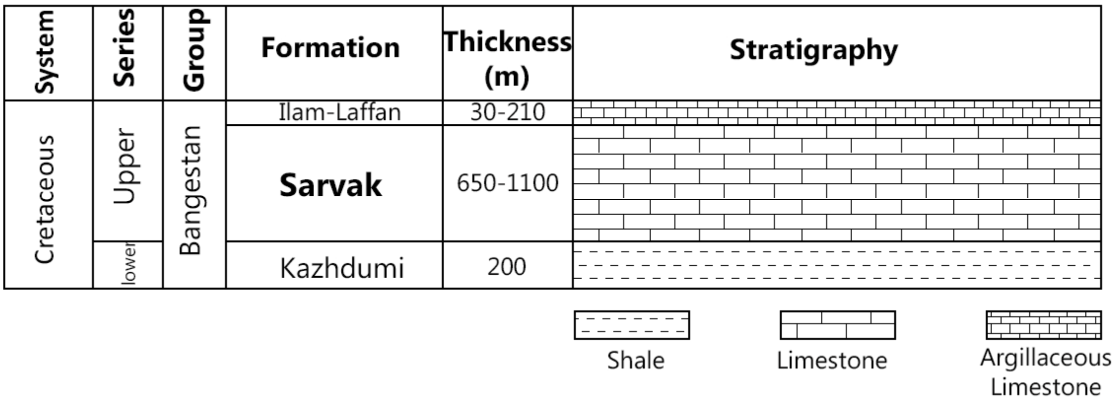

Figure 1. Simplified stratigraphy of the Sarvak formation depicting the major lithological successions and the thickness of the upper and lower formations (Adapted from Abdollahie Fard et al., 2006).

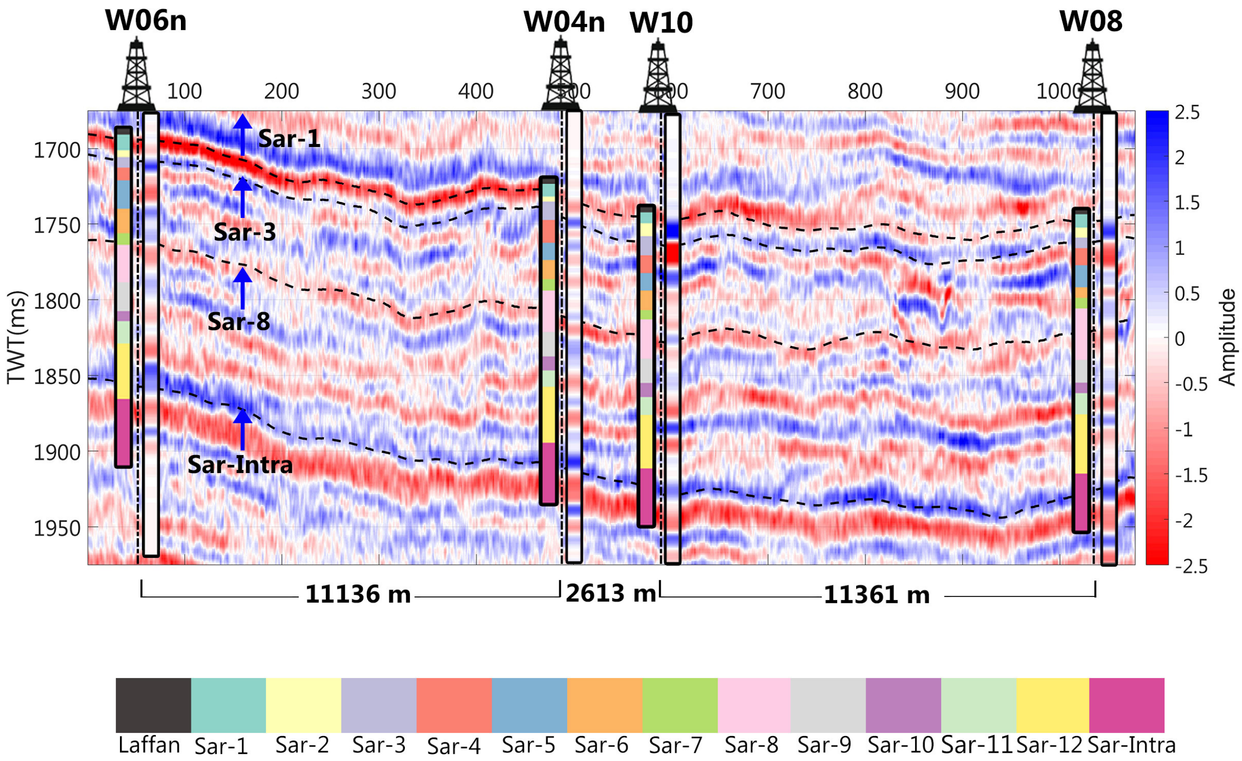

Figure 2. The 2D seismic profile is superimposed by the well locations, their distance, their associated well-to-seismic ties, the tops of the reservoir subzones (color-coded columns), as well as the horizons' TWT of four reservoir subzones (Sar-1, 3, 8, and Intra) with blue arrows and balck dashed lines.

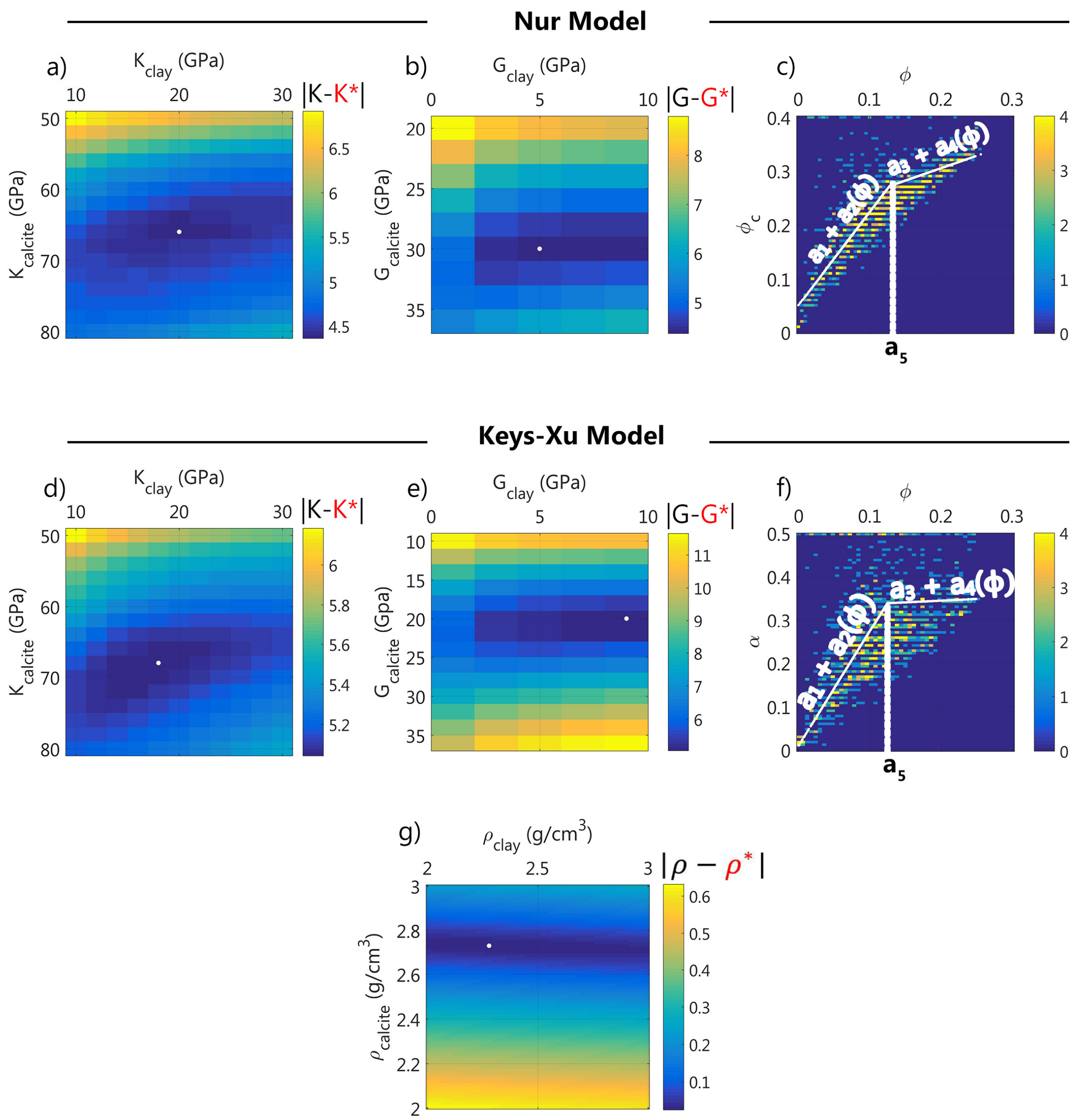

Figure 3. The error surfaces of different combinations of minerals' elastic moduli for the Nur (a and b) and the Keys-Xu (c and d) models. The error surface for minerals' density is shown in (g). The red asterisked properties in the color bars represent the modeled properties. The piecewise linear regression of the optimized critical porosity and pore aspect ratio (white dashed lines) against the porosity are shown in (c) and (f), respectively.

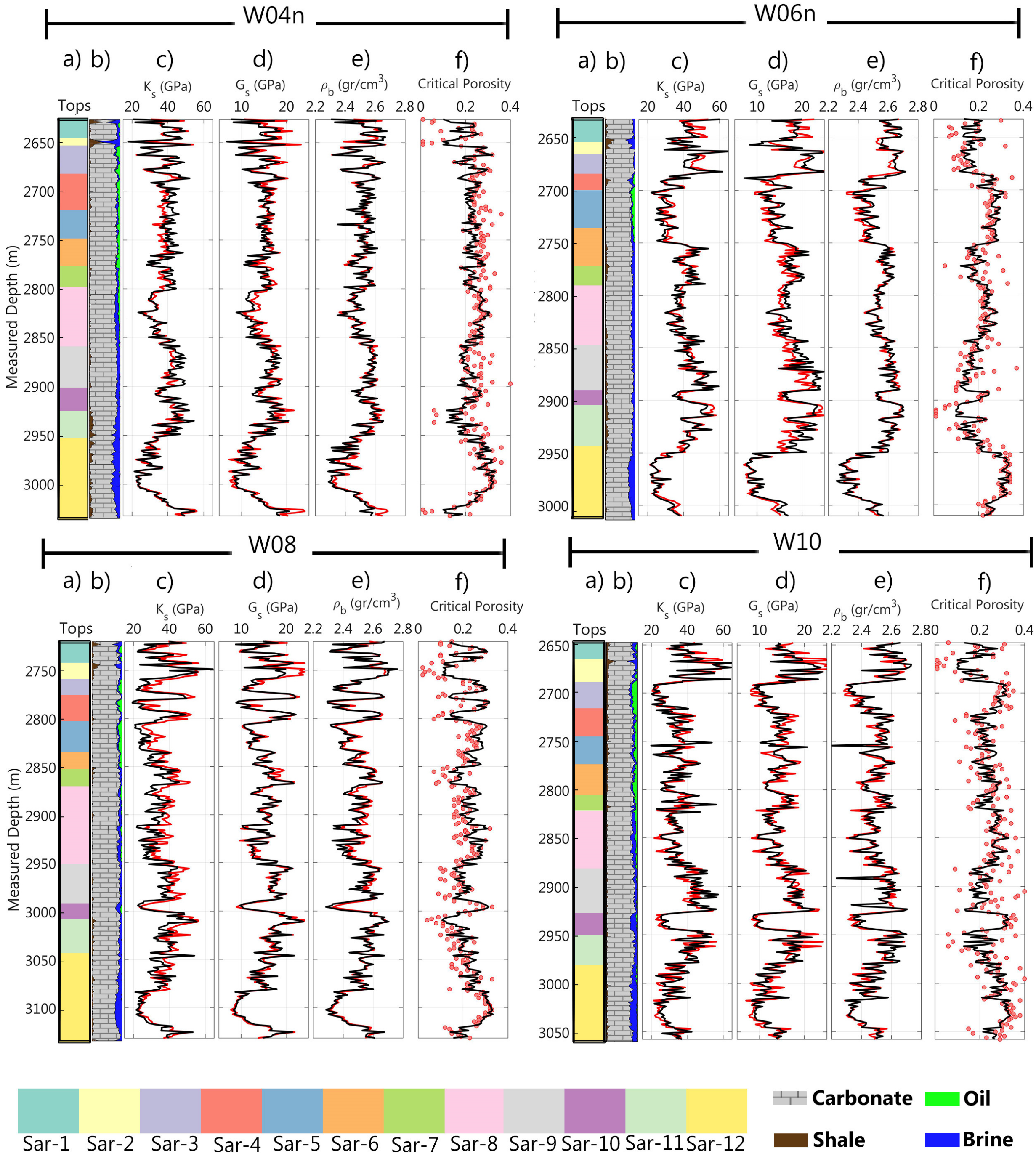

Figure 4. The results of calibration algorithm over four wells using the Nur model. (a) the color-codded tops of the reservoir subzones, (b) the lithology description. The red and black curves in (c)-(e) describe the modeled and observed properties, respectively. (c) the modeled and observed saturated bulk modulus, (d) the modeled and observed saturated shear modulus, (e) the modeled and observed bulk density. The black curves in (f) represent the result of the piecewise linear regression of the optimized critical porosity (red circles) with the effective porosity.

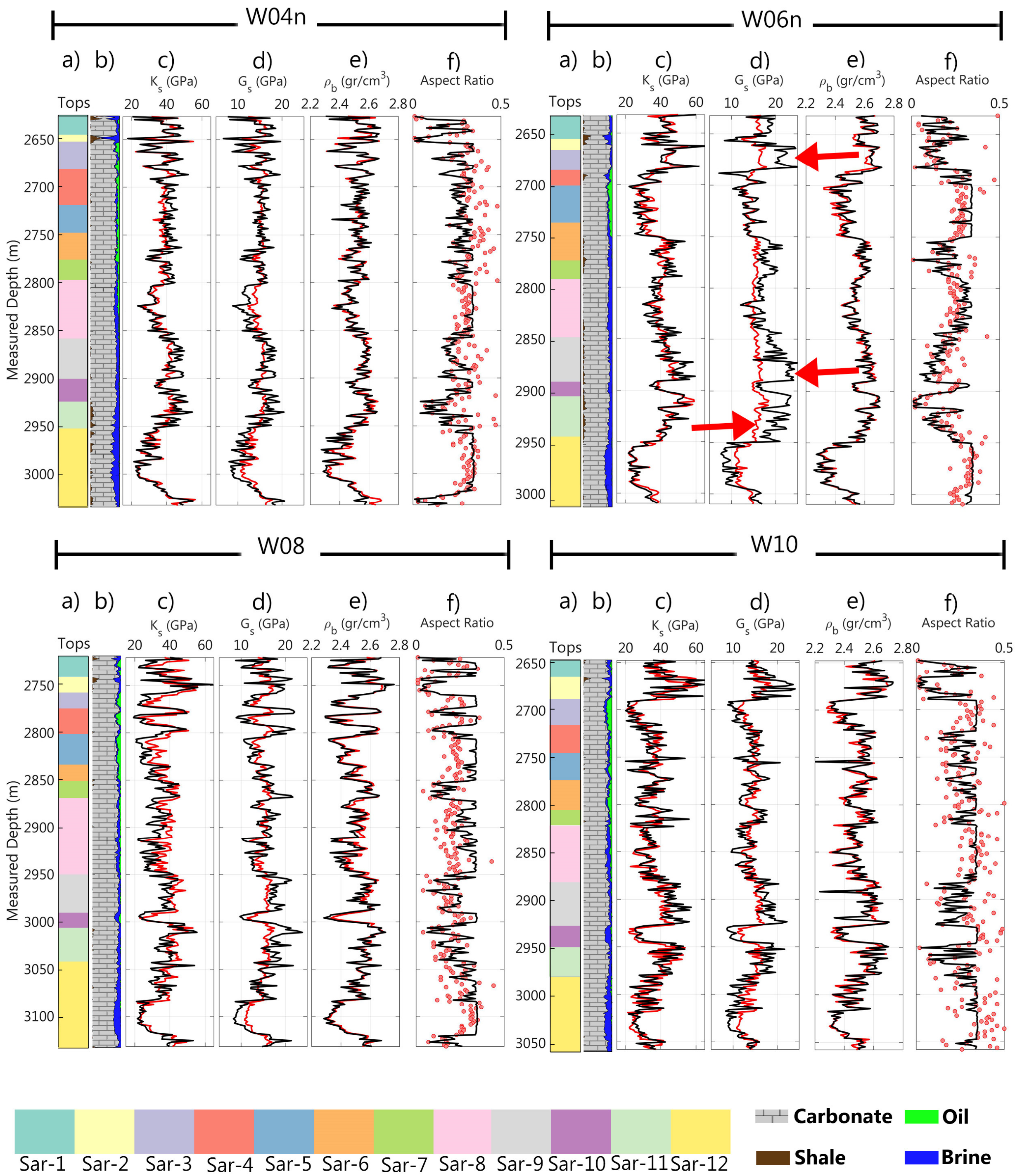

Figure 5. The results of calibration algorithm over four wells using the Keys-Xu model. The descriptions of (a)-(e) are the same as Figure 4. The black curves in (f) represent the result of the piecewise linear regression of the optimized pore aspect ratio (red circles) with effective porosity. Note (d) for well W06n, where the algorithm fails to model the observed shear moduli.

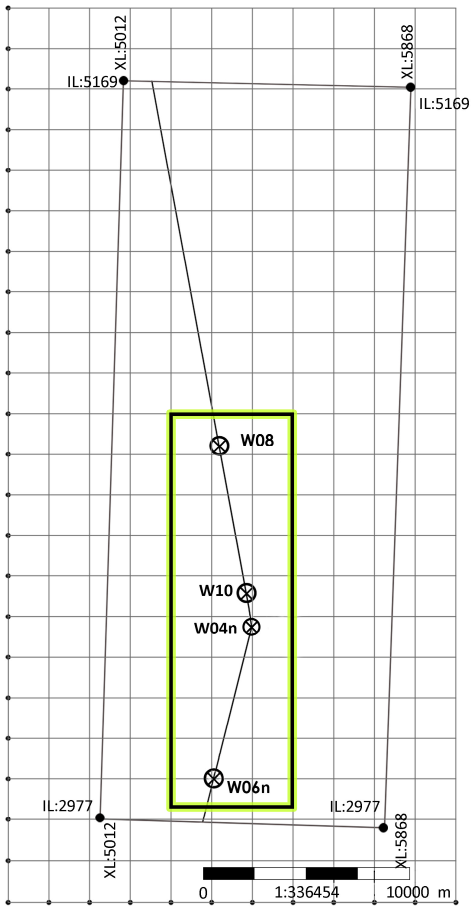

Well	X-line	Inline
W04n	5447	3550
W06n	5356	3114
W08	5332	4097
W10	5424	3652

Figure 6. The coordinates of the platform, including the range of crosslines, inlines, well locations, the crooked line passing through the wells. The rectangle with yellow borders specifies the coordinates of extracted seismic data for the 3D inversion.

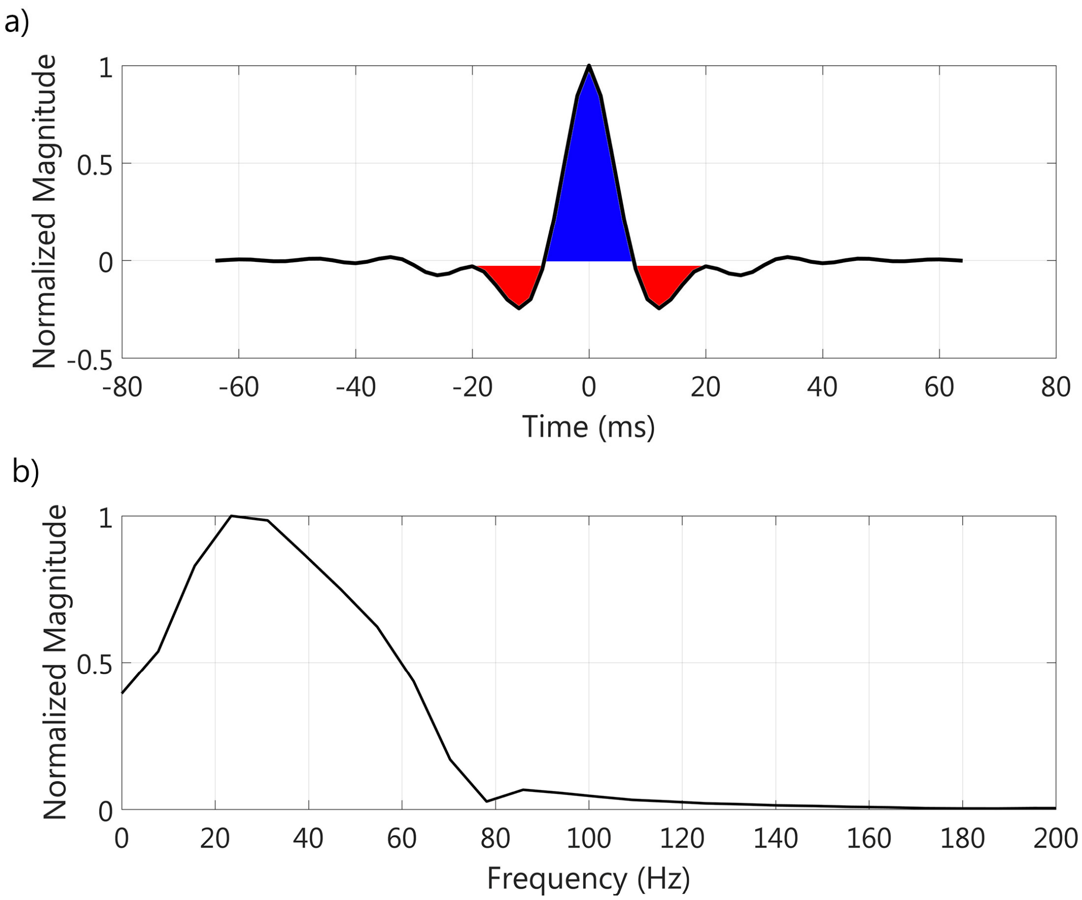

Figure 7. The extracted statistical wavelet (a), and its associated frequency spectrum (b).

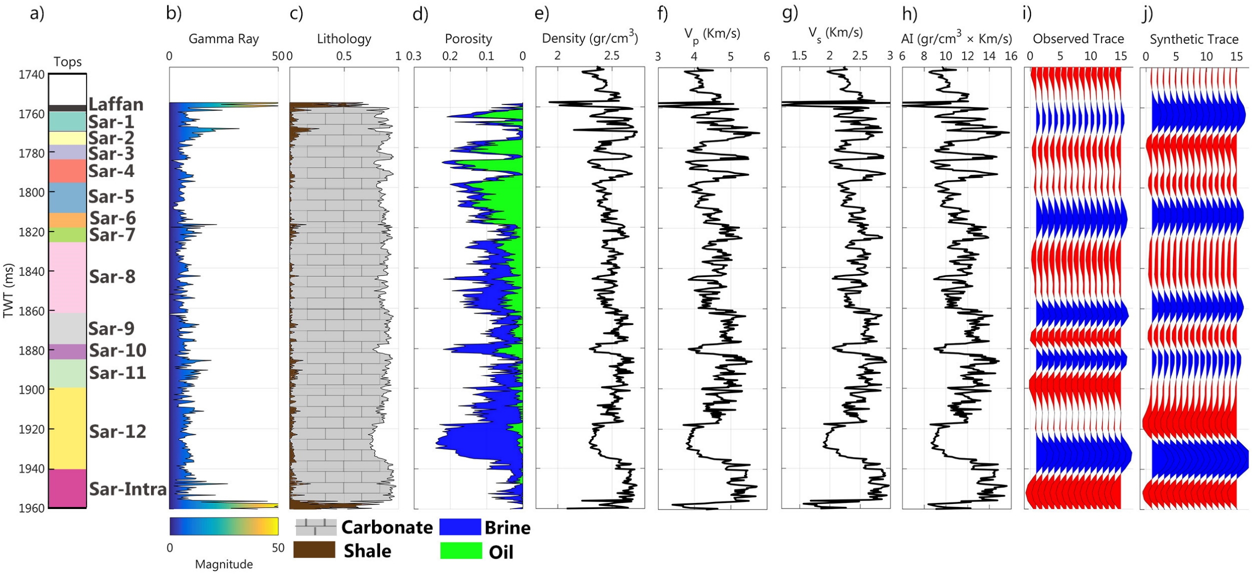

Figure 8. Description of the available sonic and petrophysical logs for well W08, (a) the tops of the subzones, (b) the gamma-ray log, (c) the lithology column, (d) the porosity log describing the oil and brine accumulation, (e) the density log, (f) the compressional velocity log, (g) the shear velocity log, (h) the acoustic impedance, (i) the synthetic trace constructed through the well-to-seismic tie, (j) the observed trace at well location.

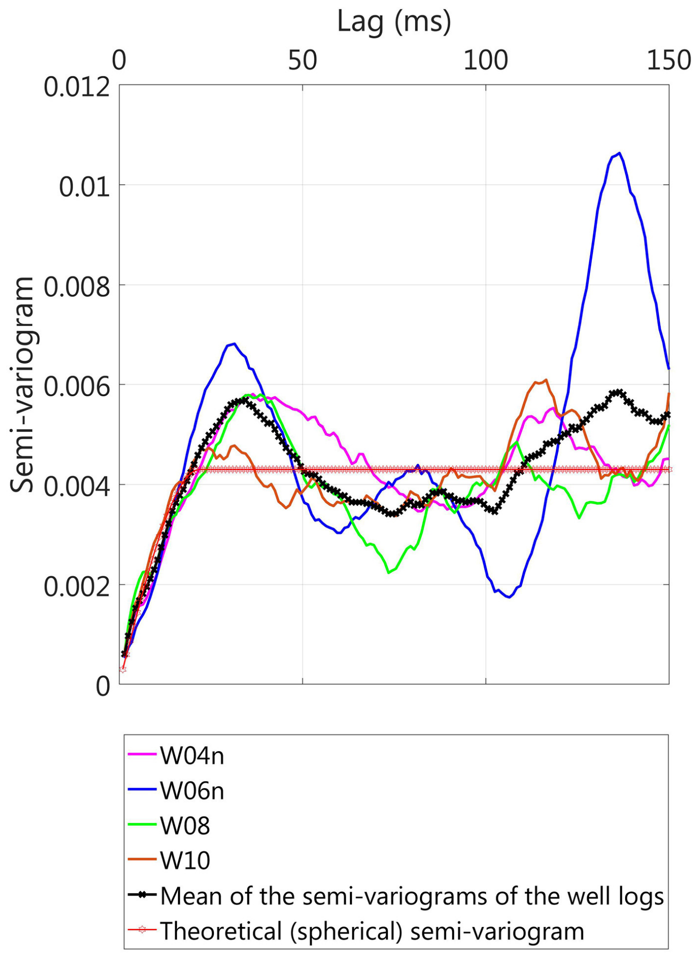

Figure 9. The semi-variograms of the porosity logs (colored lines), their mean (black line), and the fitted theoretical semi-variogram on the mean semi-variogram (red line).

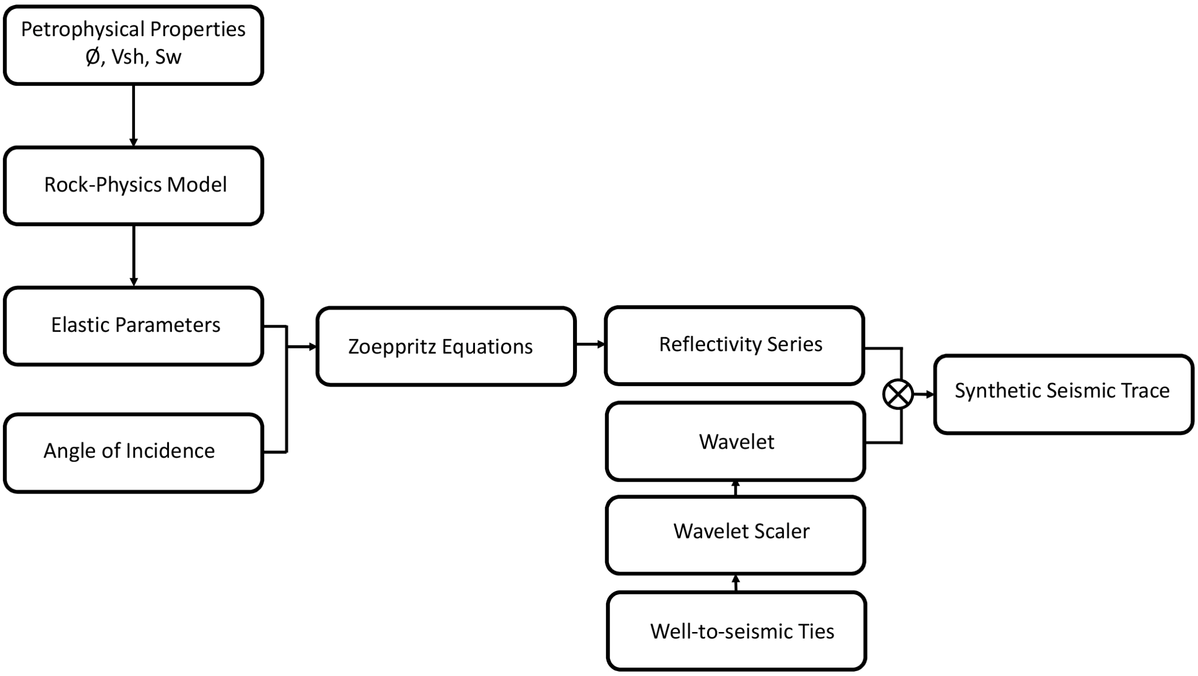

Figure 10. The 1D convolution procedure to generate the synthetic seismic trace.

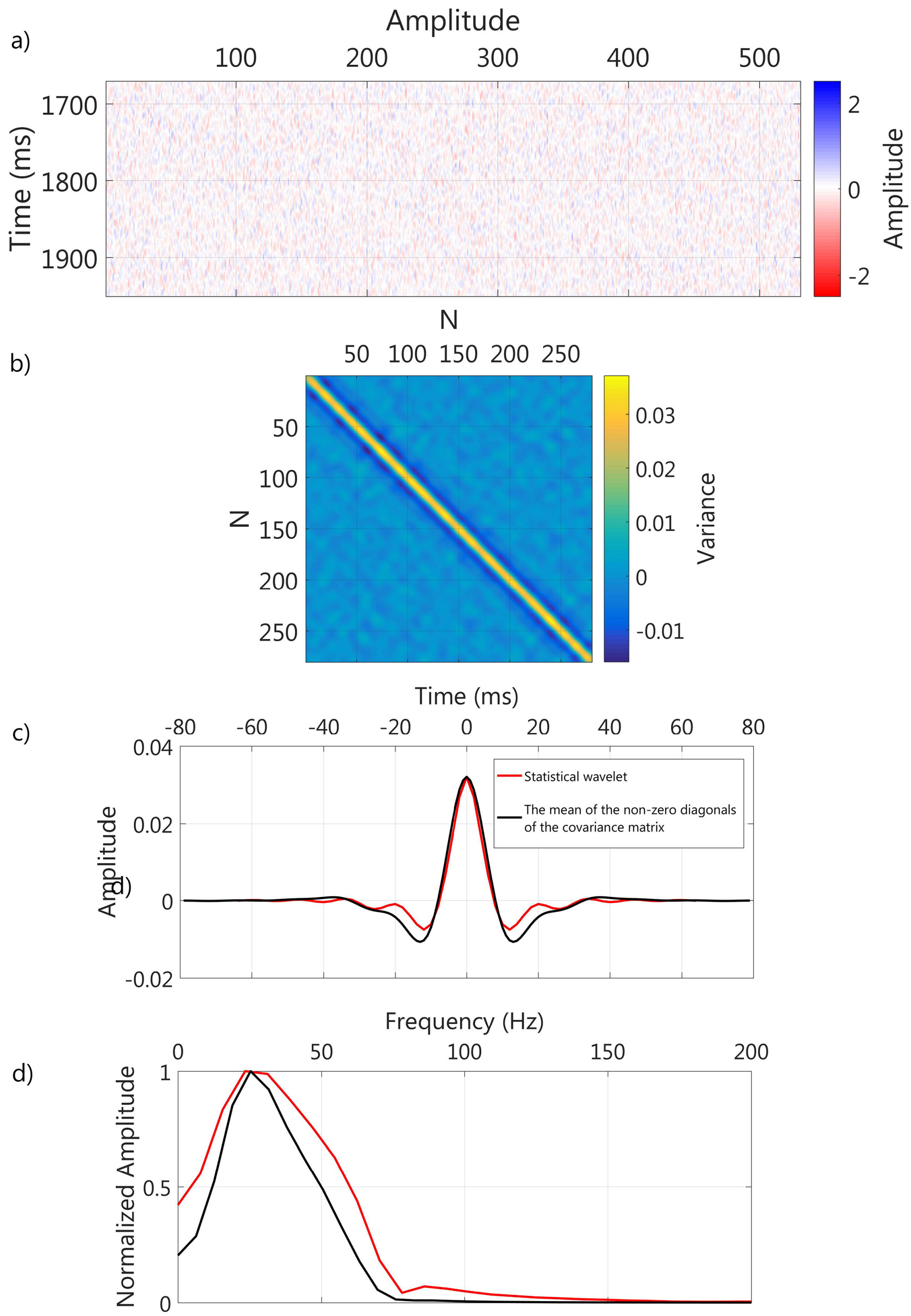

Figure 11. The description of the correlated Gaussian noise used in probabilistic seismic inversion, (a) 2D bandlimited Gaussian random filed constructed through convolution of the statistical seismic wavelet with the 2D Gaussian random reflectivity series with mean zero and variance of 0.0324 (Gaussian noise), (b) the covariance matrix of the correlated noise in (a), (c) the statistical seismic wavelet (red) with the mean of the non-zero diagonals of the covariance matrix (black), (d) the frequency spectrum of the wavelets in (c).

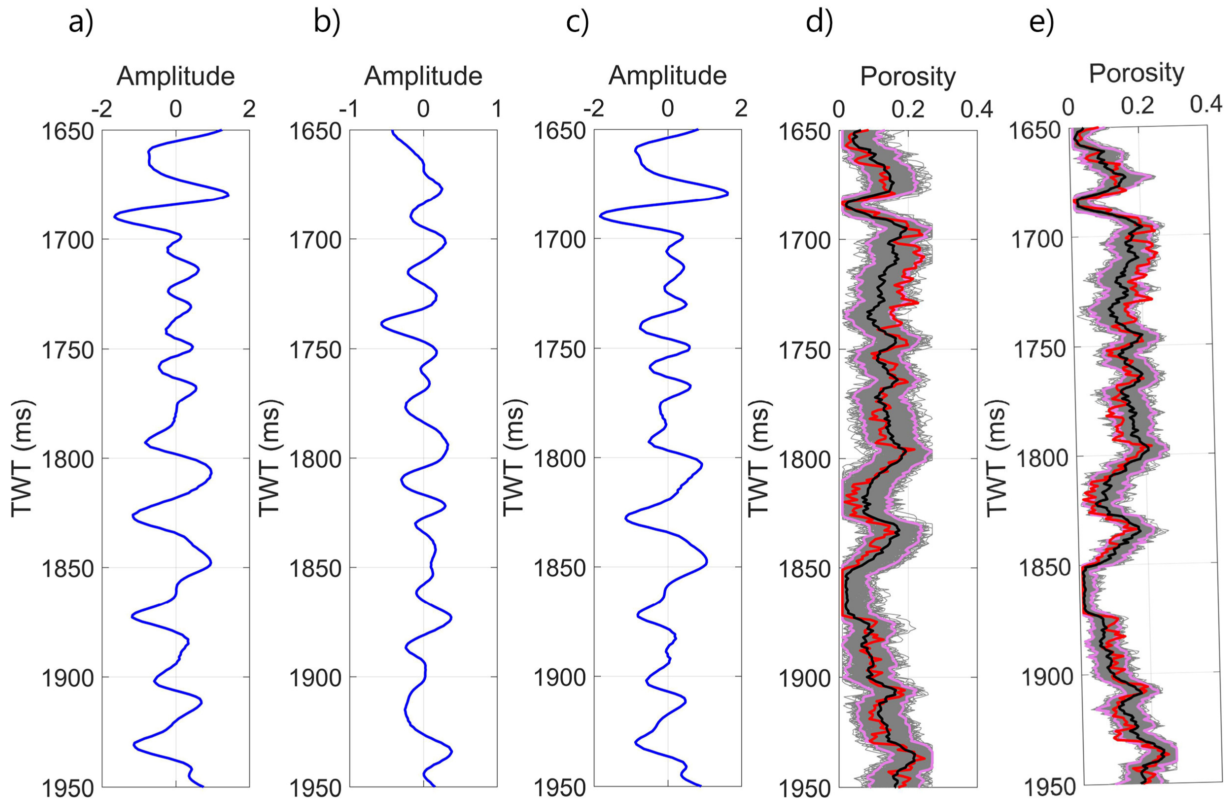

Figure 12. (a) the noise-free synthetic seismic trace, (b) the band-limited Gaussian noise, (c) the noisy seismic trace, (d) the result of probabilistic inversion of noisy seismic trace assuming correlated noise in inversion (Case A), (e) the result of probabilistic inversion of noisy seismic trace assuming uncorrelated noise in inversion (Case B). The porosity realizations, their mean, and the true porosity are shown with grayish, black, and red lines.

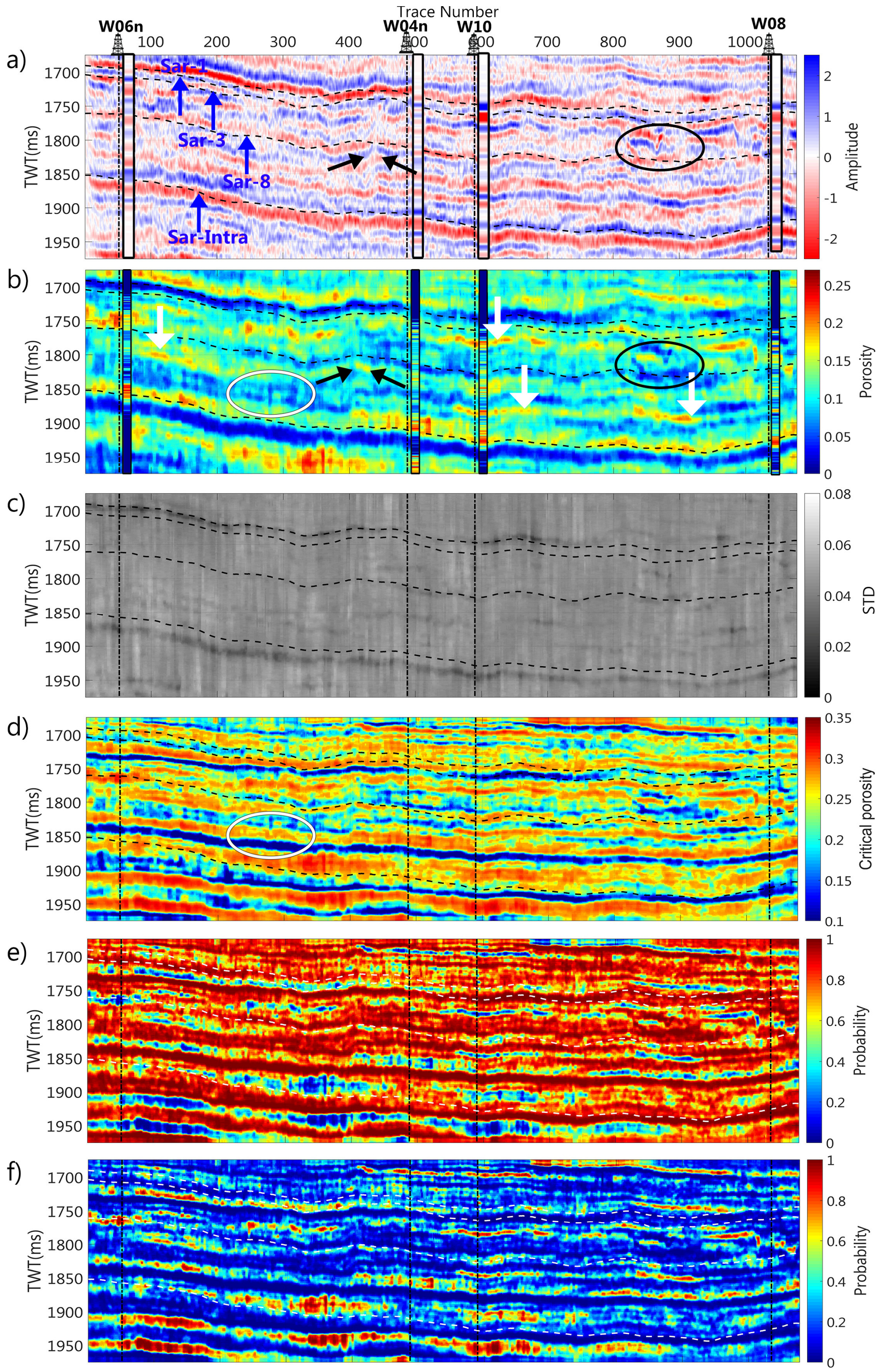

Figure 13. The probabilistic inversion results using thr Nur rock-physics model, (a) the seismic data superimposed by well-to-seismic tie results and the horizons' TWT of Sar-1, 3, 8, and Intra subzones (black dashed lines flagged by blue arrows), (b) the porosity posterior mean model, (c) the standard deviation of the porosity realizations, (d) the critical porosity obtained through converting the mean porosity model via the optimized regression coefficients of rock-physics modeling, (e) the facies probability with a porosity between zero and 0.15. (f) the facies probability with a porosity between 0.15 and 0.3. Some events are flagged by arrows and ellipses to compare the inversion performance (refer to the text).

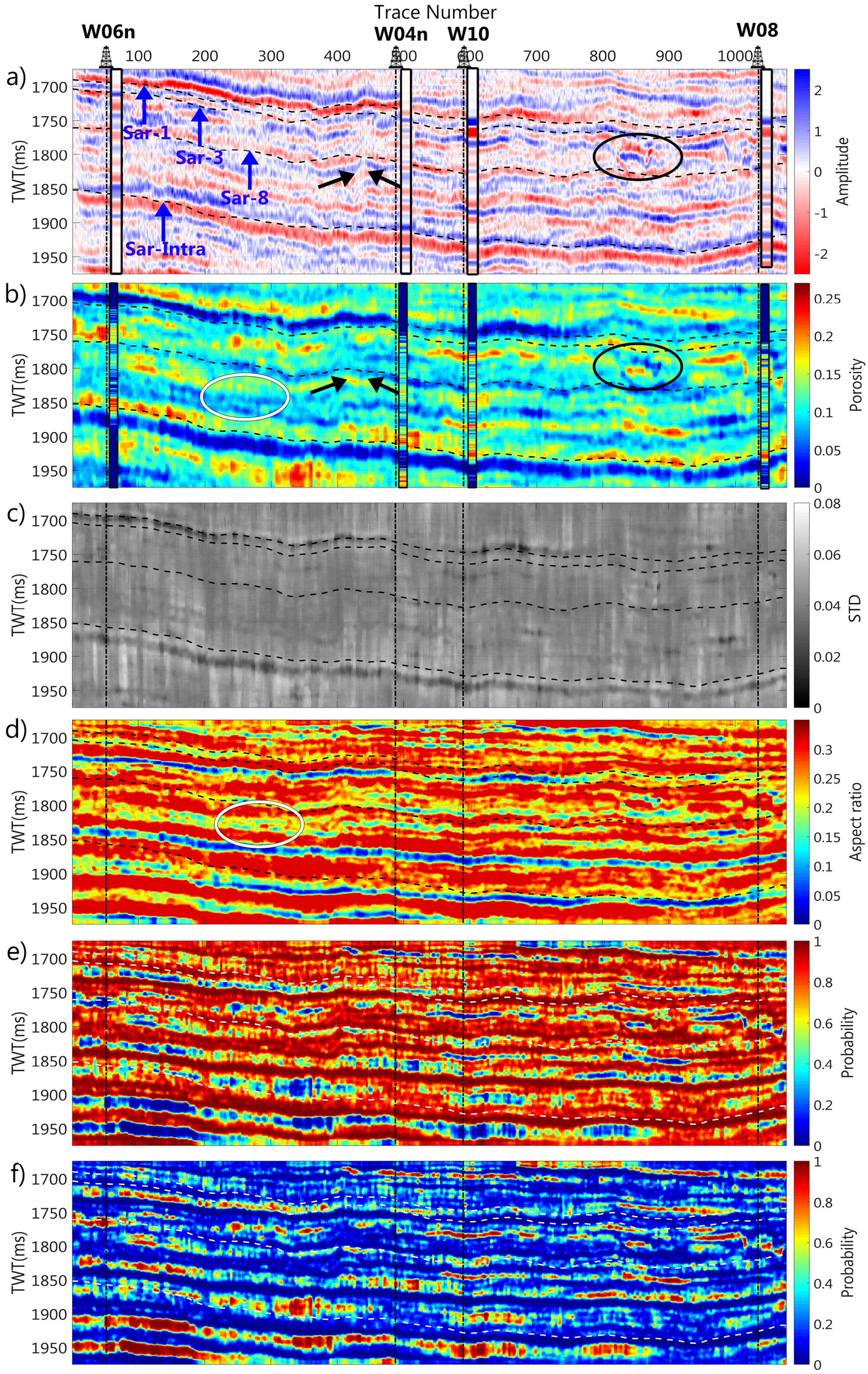

Figure 14. The probabilistic inversion results using the Keys-Xu rock-physics model, the descriptions of (a), (b), (c), (e), and (f) are the same as in Figure 13. (d) represents the pointwise pore aspect ratio model.

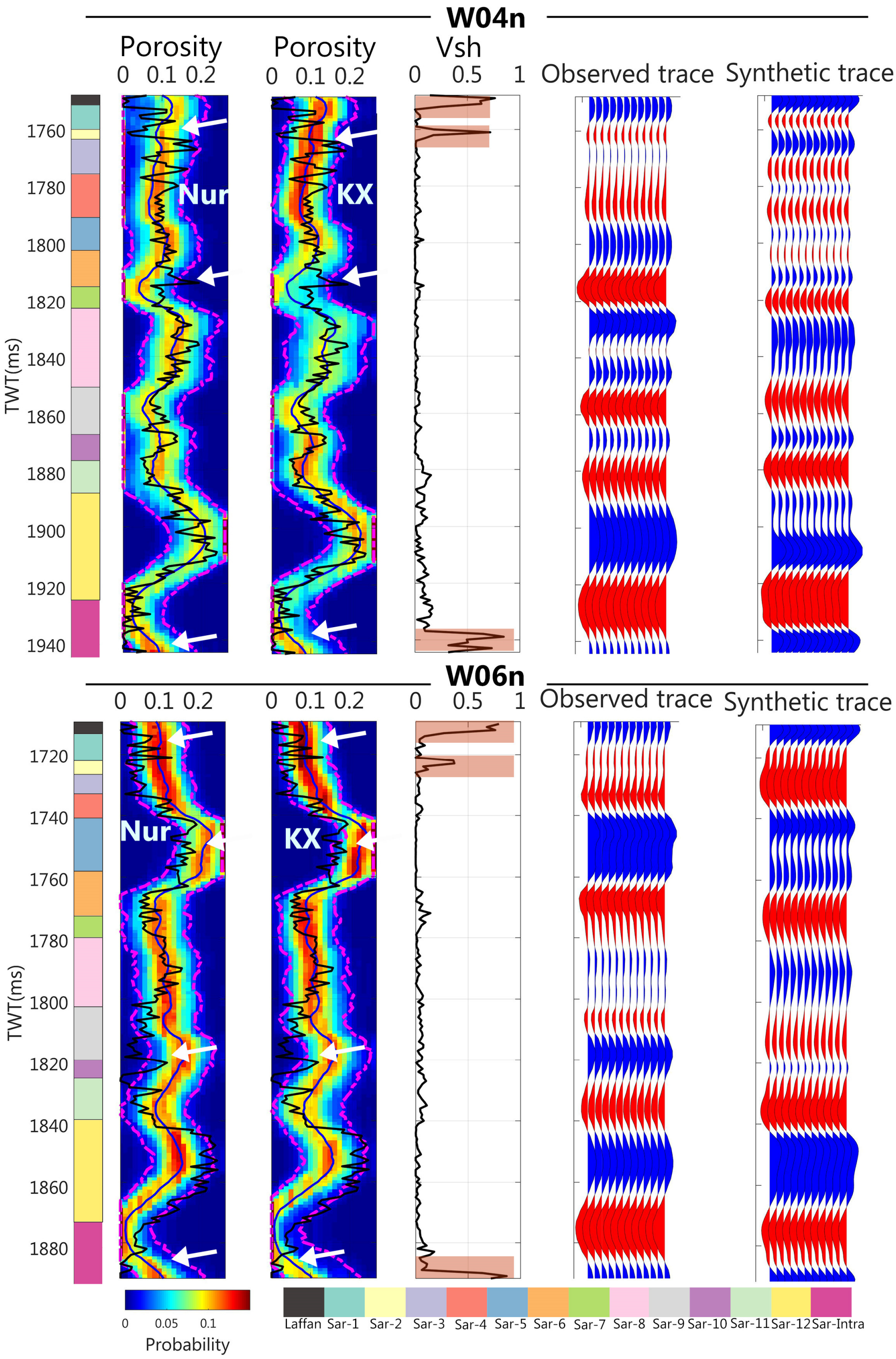

Figure 15 part a. The inversion results in well locations for wells W04n and W06n using both Nur and Keys-Xu rock-physics models. From left to right: The color-coded column represents the TWT of the top of the subzones. The porosity realizations are shown as the density plots superimposed by the true porosity log (black), the mean of the porosity realizations (blue), and the 95% confidence interval (pink dashed lines). The colored background shows the probability at each time sample. The three last columns show the shale volume, the observed trace, and synthetic trace in well location. White arrows represents the regions, where the inversion fails to capture the true porosity.

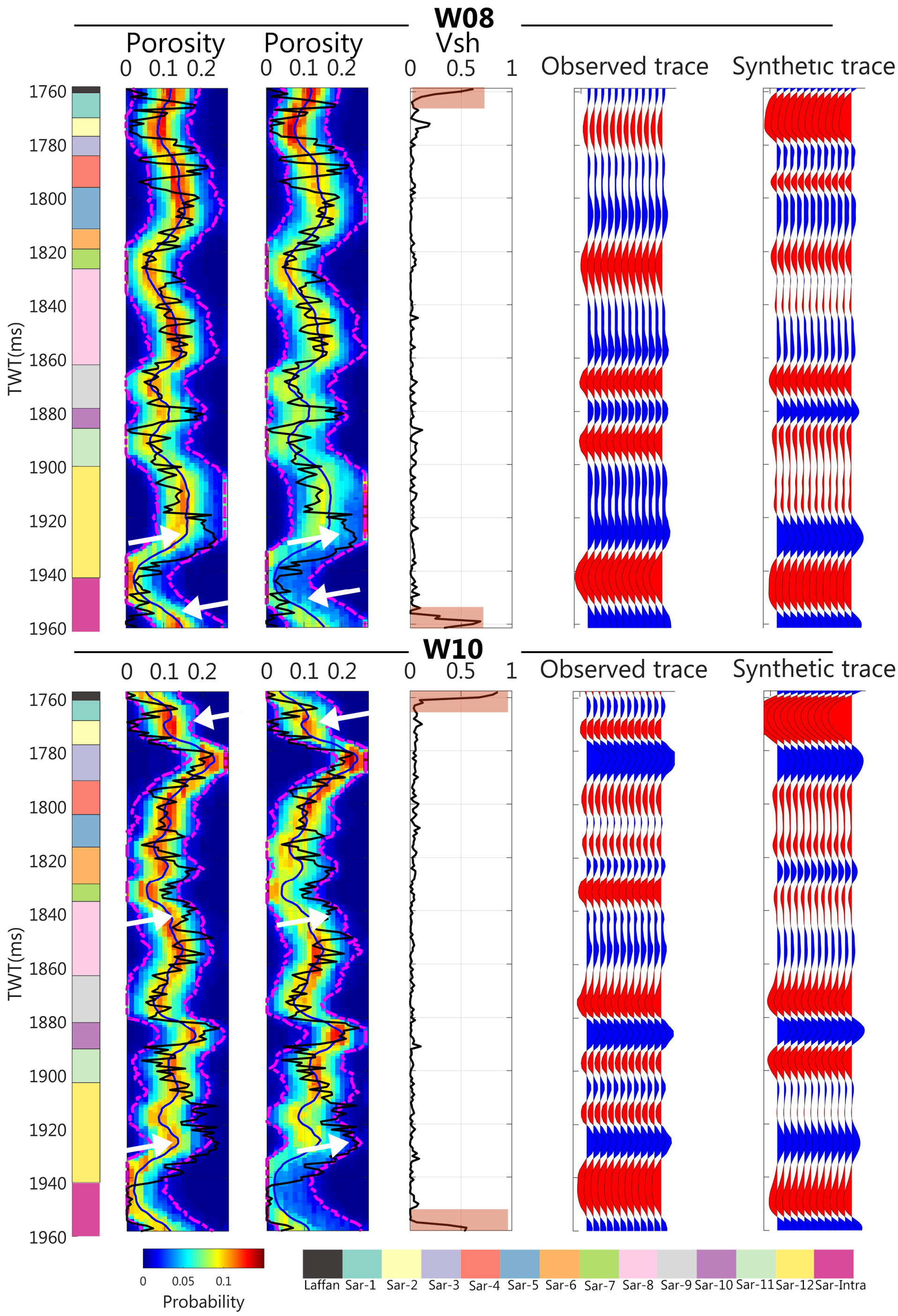

Figure 15 part b. The inversion results in well locations for wells W08n and W10 using both Nur and Keys-Xu rock-physics models.

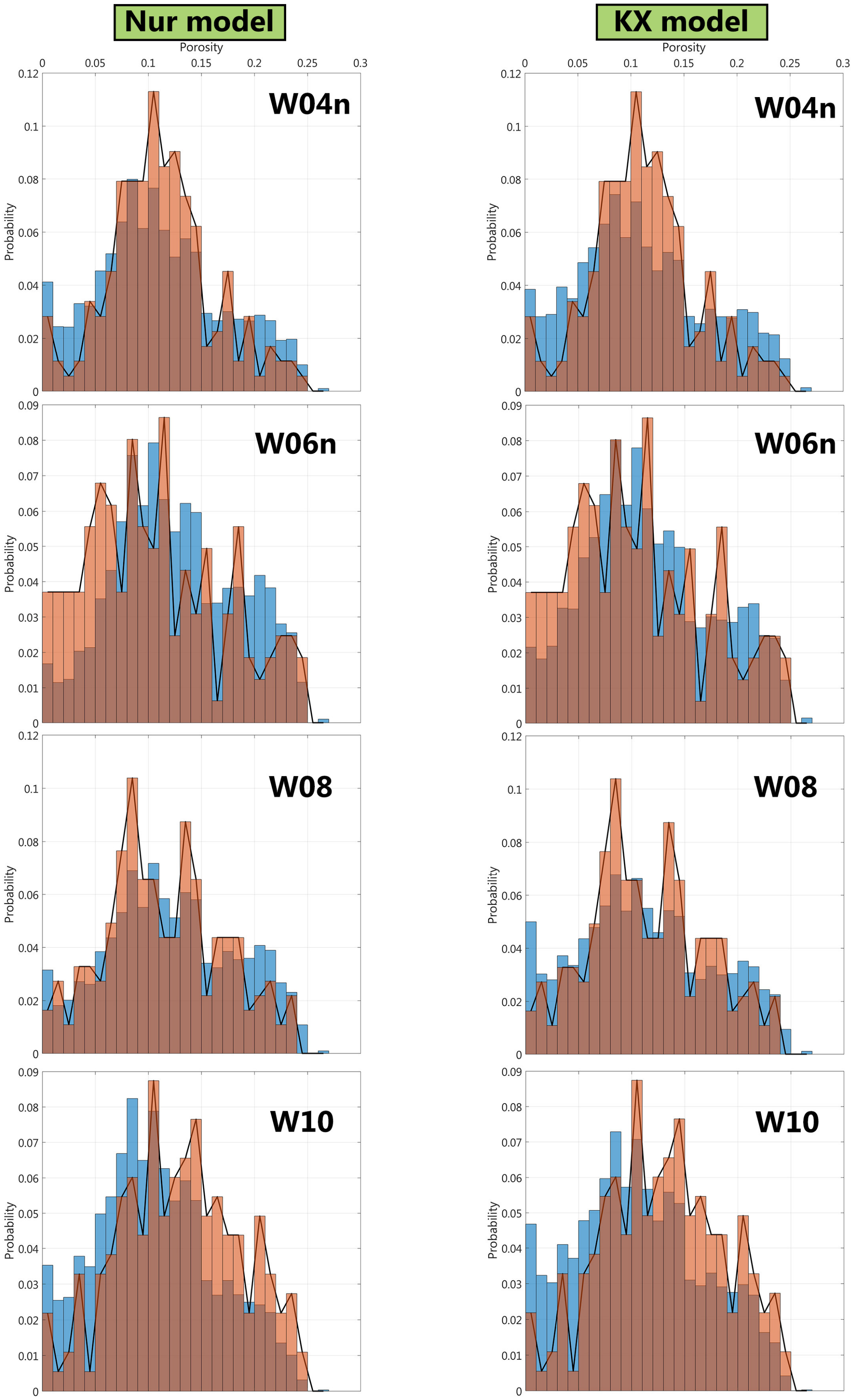

Figure 16. The 1D marginal distributions of the porosity realizations (blue boxes) and the histogram of the porosity logs (brown boxes) for the four well logs using two rock-physics models in inversion.

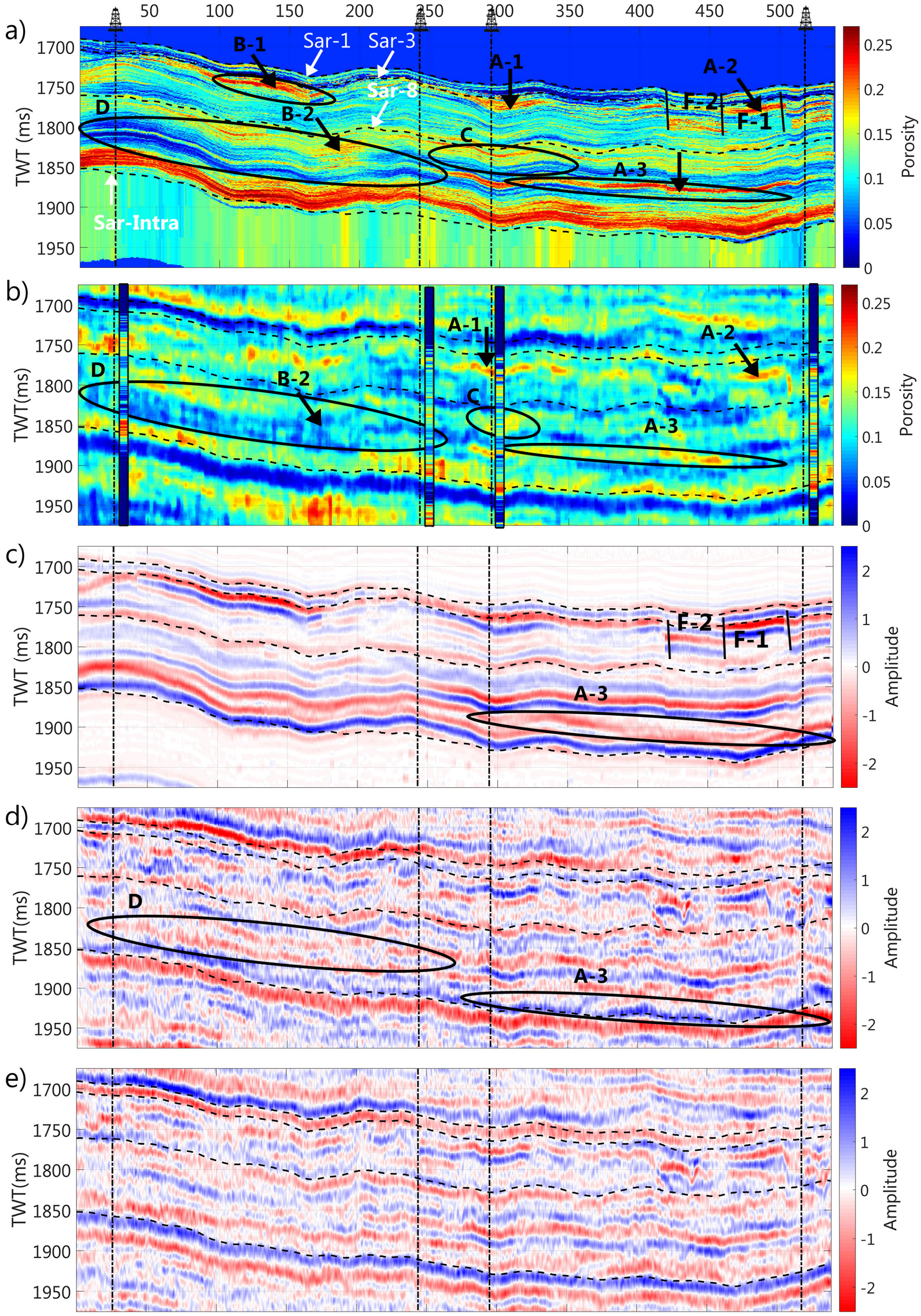

Figure 17. Comparison of the geological model constructed through geostatistical approach (sequential Gaussian simulation) by the client and the porosity model obtained by the single-step probabilistic seismic inversion (b). The associated seismic responses with the models in (a) and (b) are shown in (c) and (e). The observed seismic data is demonstrated in (d). See the text for more details of the description of the flagged features on these figures.

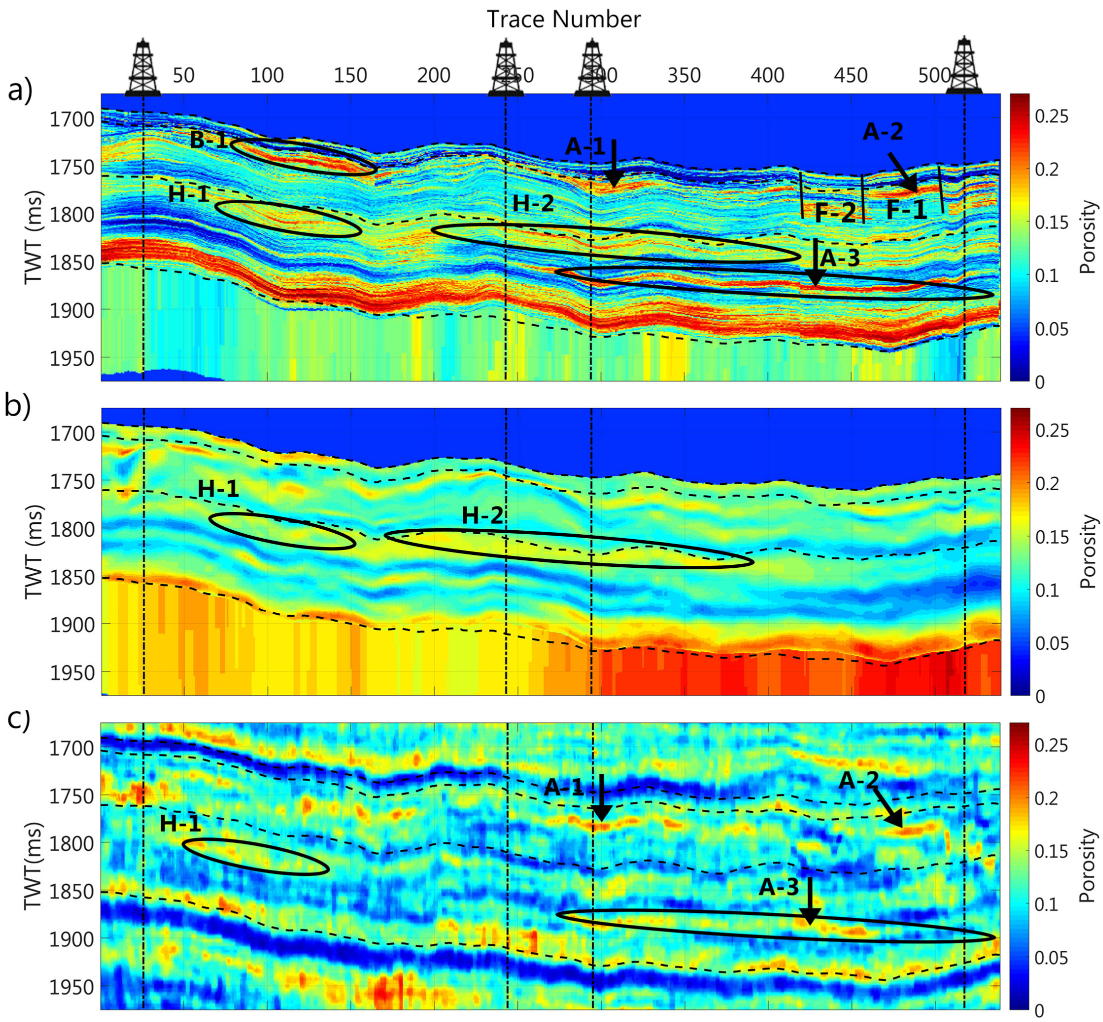

Figure 18. The porosity models obtained through (a) geostatistical (sequential Gaussian simulation) approach, (b) a two-step deterministic seismic inversion provided by the clinet, and (c) the single-step probabilistic seismic inversion. The geological model in (a) has been constrained laterally to the porosity model in (b) in the simulation procedure.

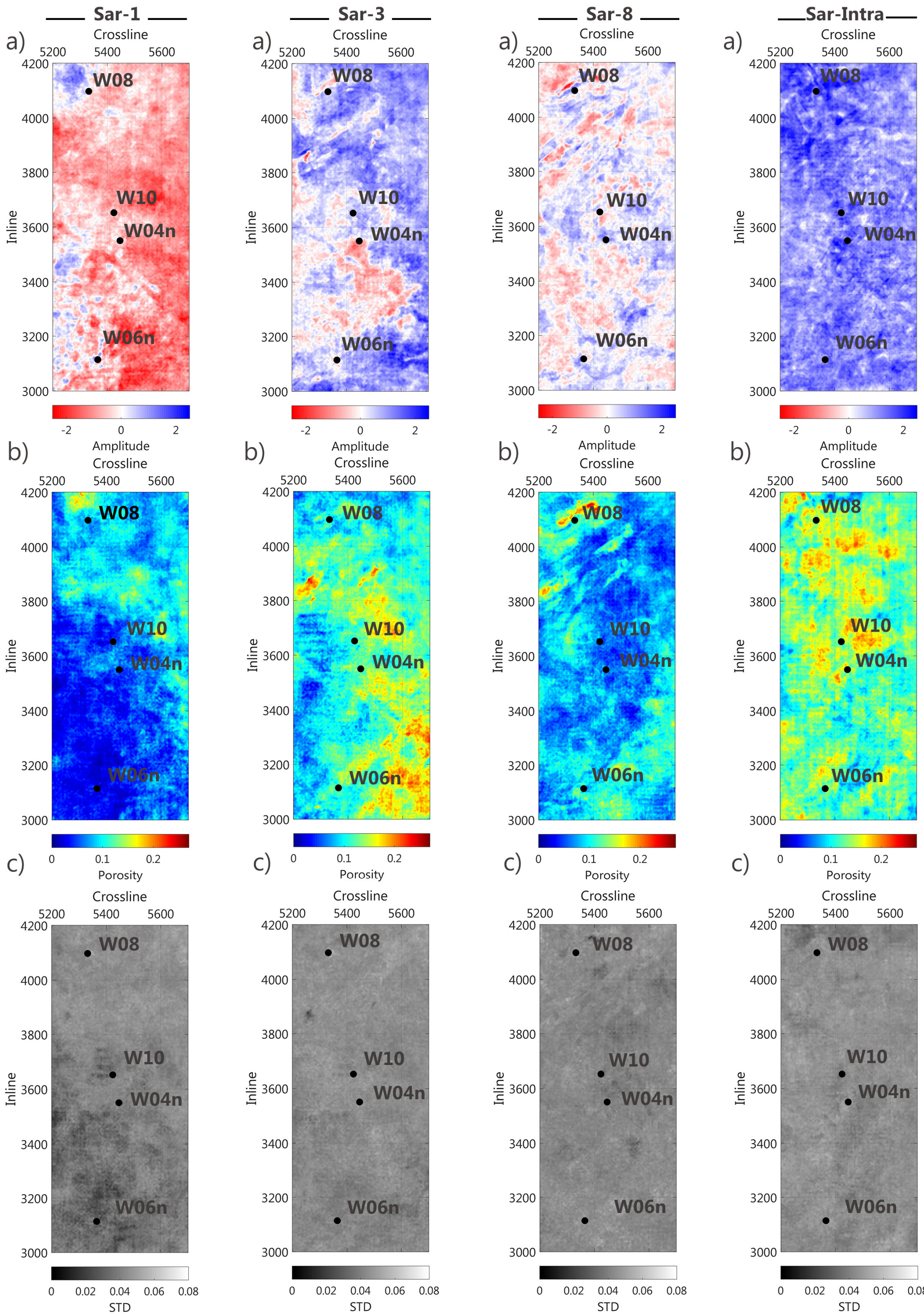

Figure 19. The time maps of (a) seismic amplitudes, (b) the mean porosity models obtained by the probabilistic inversion, and (c) the standard deviation models of the porosity realizations for the Sar-1, 3, 8, and Intra subzones. The locations of four wells are superimposed on each time map.

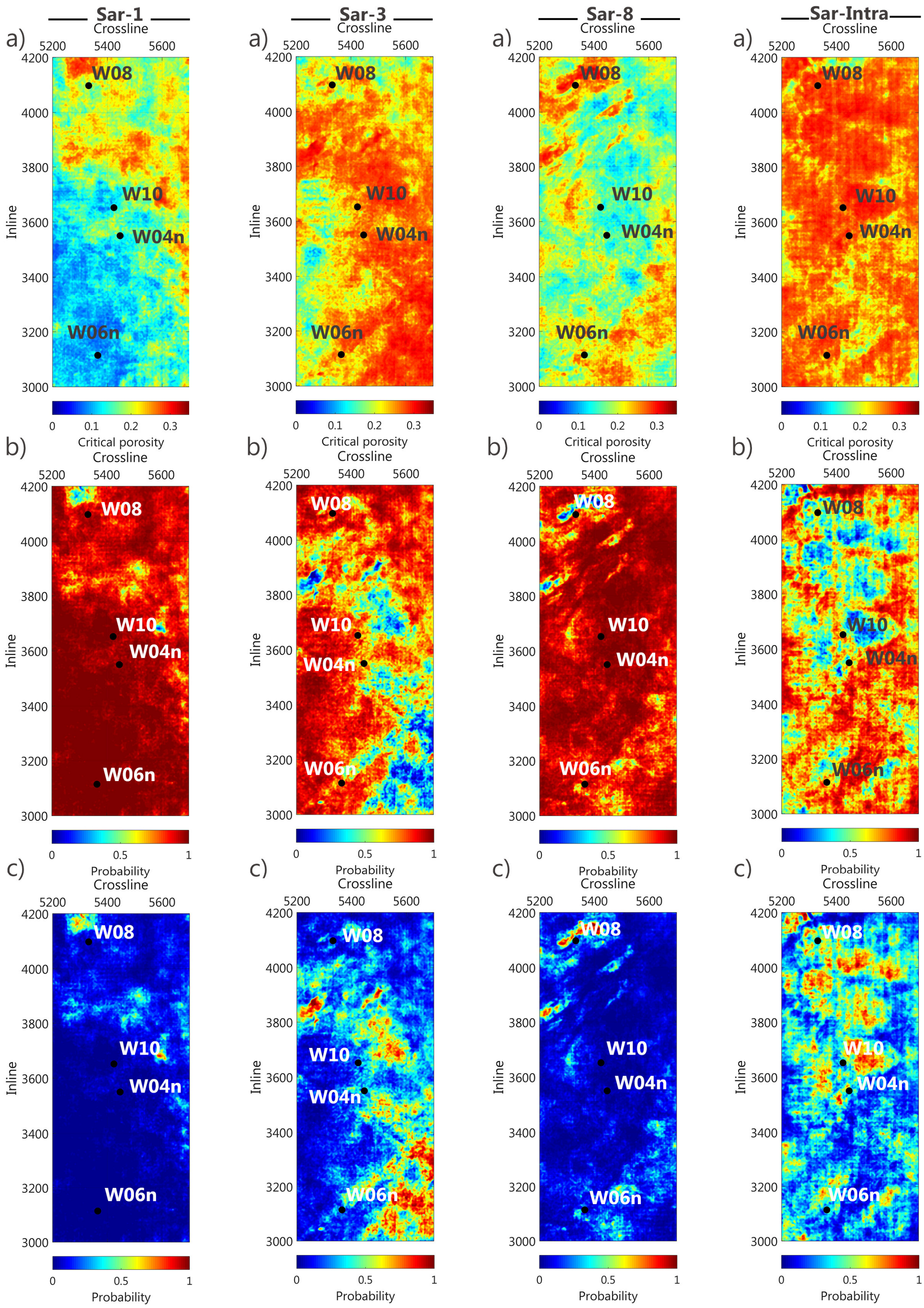

Figure 20. The time maps of (a) the critical porosity, (b) the probability of the facies-1, where porosity is less than 0.15, (c) the probability of the facies-2, where porosity varies between 0.15 and 0.3, for the Sar-1, 3, 8, and Intra subzones. The locations of four wells are superimposed on each time map.

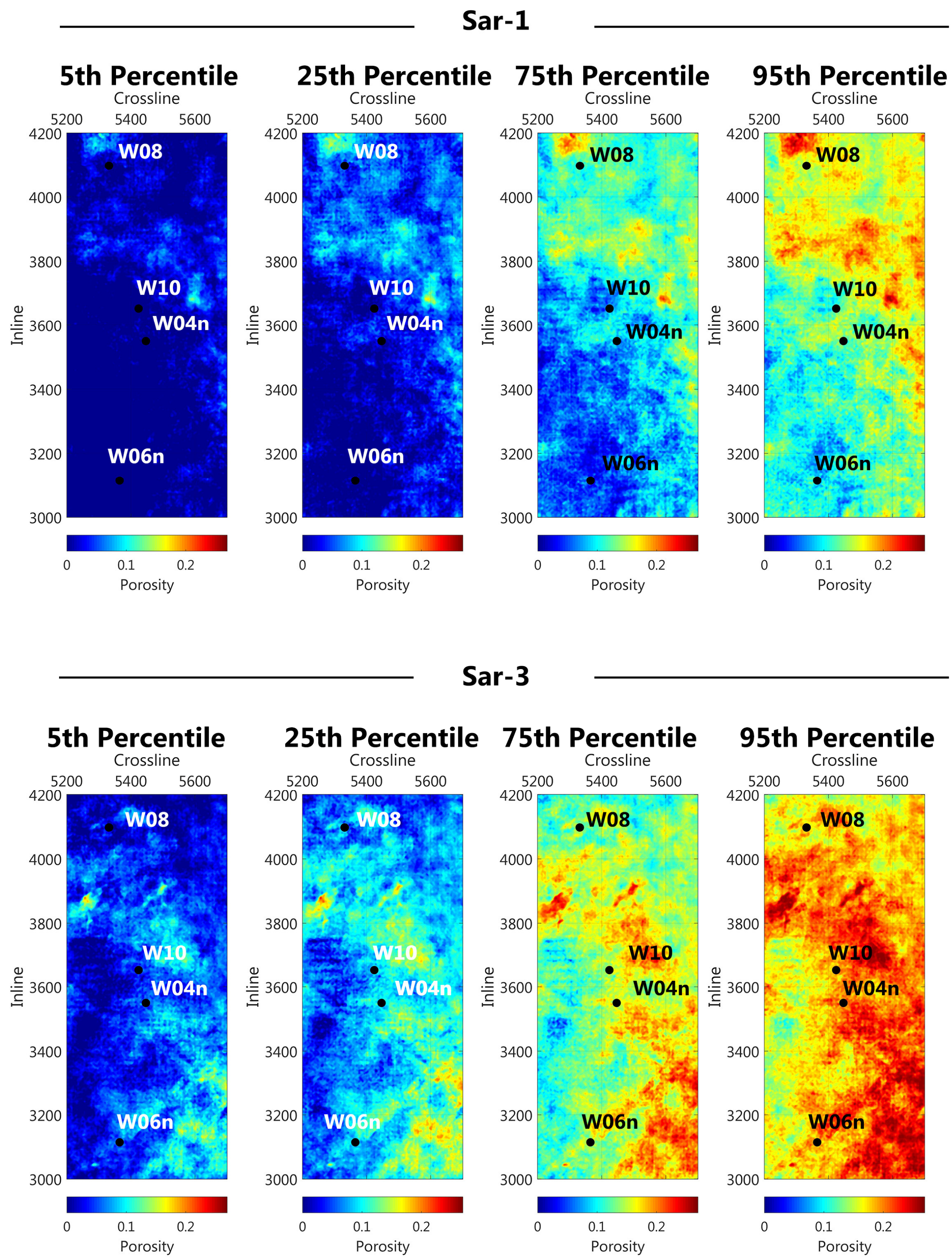

Figure 21. The 5th, 25th, 75th, and 95th percentiles for the Sar-1 subzone (top row) and the Sar-3 subzone (bottom row).

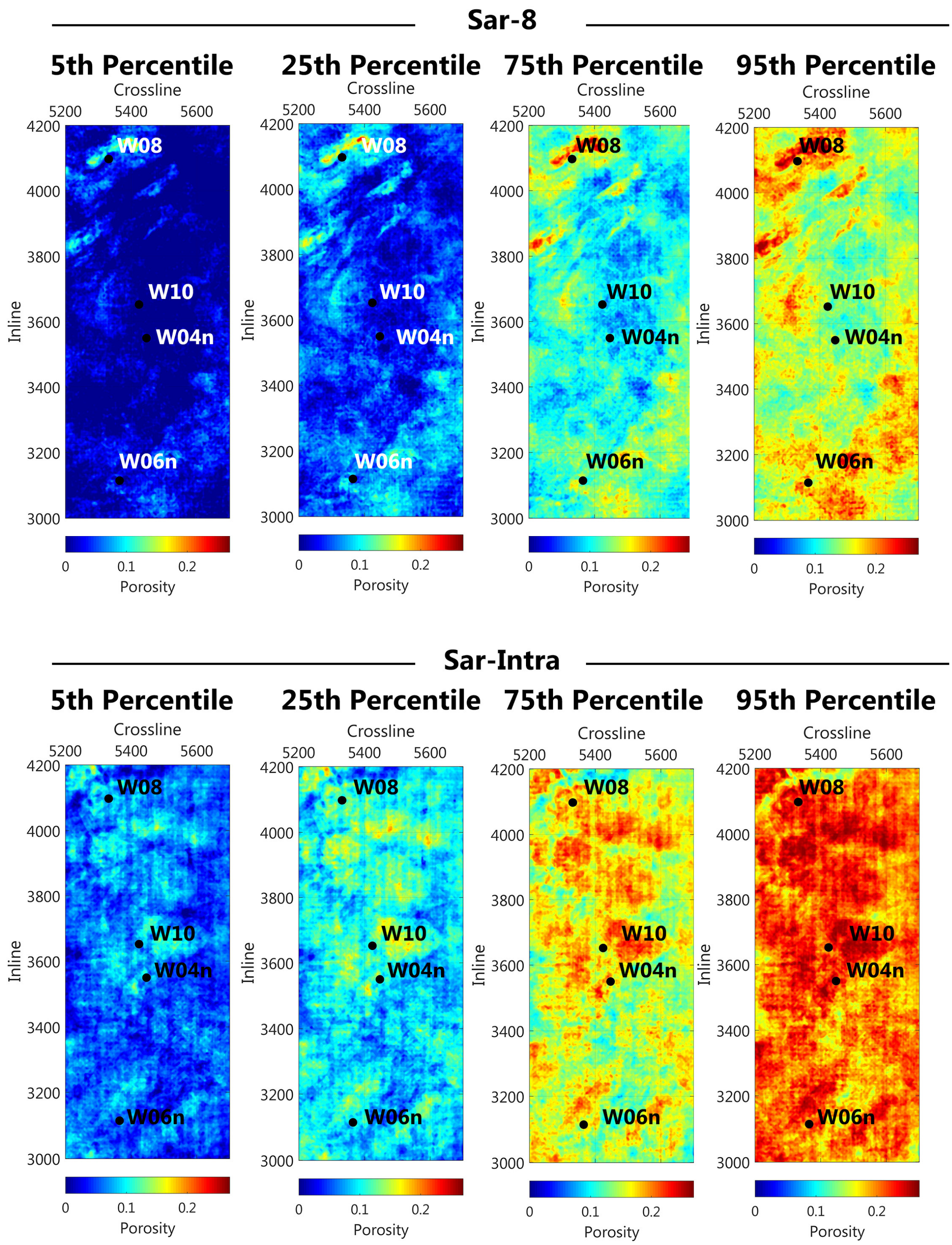

Figure 22. The 5th, 25th, 75th, and 95th percentiles for the Sar-8 subzone (top row) and the Sar-Intra subzone (bottom row).